Article

Cell Reports

The Replisome Mediates A-NHEJ Repair of Telomeres Lacking POT1-TPP1 Independently of MRN Function

Graphical Abstract

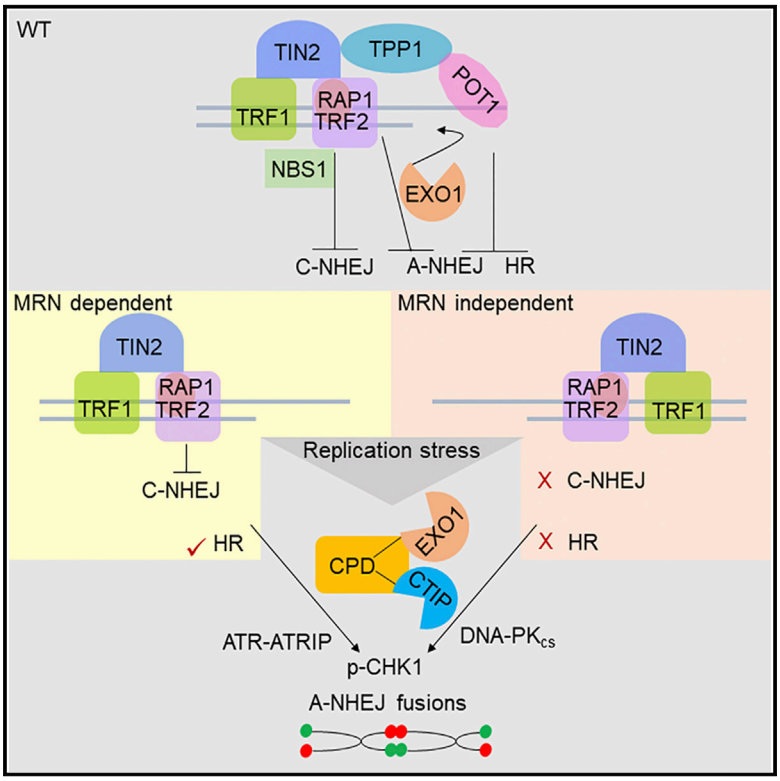

Highlights

- A-NHEJ repair of telomeres lacking POT1-TPP1 occurs independently of MRN
- Without MRN, Claspin and DNA-PK$_{cs}$ promote CHK1 phosphorylation and A-NHEJ repair
- Claspin interacts with TRF2 and helps recruit EXO1 for telomere C-strand resection
- Increased replication stress in tumors without POT1 stabilized by claspin

Authors

Rekha Rai, Peili Gu, Cayla Broton, Chandan Kumar-Sinha, Yong Chen, Sandy Chang

Correspondence

rekha.rai@yale.edu (R.R.), s.chang@yale.edu (S.C.)

In Brief

Rai et al. define roles for the DNA replisome components Claspin, PCNA, and DONSON in the sensing and repair of telomeres lacking POT1-TPP1. In cells lacking MRN, CPD initiates DNA-PK$_{cs}$-mediated p-CHK1 activation and A-NHEJ repair. Claspin directly interacts with TRF2 and recruits EXO1 to promote 5′ C-strand end resection.

Rai et al., 2019, Cell Reports *29*, 3708–3725
December 10, 2019
https://doi.org/10.1016/j.celrep.2019.11.012

CellPress

OPEN ACCESS
CellPress

Cell Reports
Article

The Replisome Mediates A-NHEJ Repair of Telomeres Lacking POT1-TPP1 Independently of MRN Function

Rekha Rai,[1,*] Peili Gu,[1] Cayla Broton,[1,4] Chandan Kumar-Sinha,[5] Yong Chen,[6] and Sandy Chang[1,2,3,7,*]
[1]Departments of Laboratory Medicine, Yale University School of Medicine, 330 Cedar St., New Haven, CT 06520, USA
[2]Department of Pathology, Yale University School of Medicine, 330 Cedar St., New Haven, CT 06520, USA
[3]Department of Molecular Biophysics and Biochemistry, Yale University School of Medicine, 330 Cedar St., New Haven, CT 06520, USA
[4]Tri-Institutional MD/PhD Program, Weill Cornell Medical College, New York, NY 10065, USA
[5]Department of Pathology, University of Michigan School of Medicine, Ann Arbor, MI 48109, USA
[6]National Center for Protein Science Shanghai, Institute of Biochemistry and Cell Biology, Chinese Academy of Sciences, 333 Haike Road, Shanghai 201210, China
[7]Lead Contact
*Correspondence: rekha.rai@yale.edu (R.R.), s.chang@yale.edu (S.C.)
https://doi.org/10.1016/j.celrep.2019.11.012

SUMMARY

Telomeres use shelterin to protect chromosome ends from activating the DNA damage sensor MRE11-RAD50-NBS1 (MRN), repressing ataxia-telangiectasia, mutated (ATM) and ATM and Rad3-related (ATR) dependent DNA damage checkpoint responses. The MRE11 nuclease is thought to be essential for the resection of the 5′ C-strand to generate the microhomologies necessary for alternative non-homologous end joining (A-NHEJ) repair. In the present study, we uncover DNA damage signaling and repair pathways engaged by components of the replisome complex to repair dysfunctional telomeres. In cells lacking MRN, single-stranded telomeric overhangs devoid of POT1-TPP1 do not recruit replication protein A (RPA), ATR-interacting protein (ATRIP), and RAD 51. Rather, components of the replisome complex, including Claspin, Proliferating cell nuclear antigen (PCNA), and Downstream neighbor of SON (DONSON), initiate DNA-PK$_{cs}$-mediated p-CHK1 activation and A-NHEJ repair. In addition, Claspin directly interacts with TRF2 and recruits EXO1 to newly replicated telomeres to promote 5′ end resection. Our data indicate that MRN is dispensable for the repair of dysfunctional telomeres lacking POT1-TPP1 and highlight the contributions of the replisome in telomere repair.

INTRODUCTION

DNA double-strand breaks (DSBs) are genotoxic lesions that threaten genomic integrity. The failure to repair DSBs has deleterious consequences, leading to chromosomal translocations and genomic instability that can progress to cell death or neoplastic transformation (Aguilera and Gómez-González, 2008; Jackson and Bartek, 2009). In mammalian cells, the DNA damage response (DDR) pathway senses, signals, and repairs the damage by activating multiple DNA checkpoint and repair pathways (Ciccia and Elledge, 2010; MacDougall et al., 2007). In mammalian cells, DSBs are repaired primarily by classical non-homologous end joining (C-NHEJ), homologous recombination (HR), or alternative non-homologous end joining (A-NHEJ) repair pathways. C-NHEJ repairs DSBs through direct ligation of the broken DNA ends, with little or no end processing, and thus is error prone (Lieber, 2010). In contrast, HR uses homologous sister chromatids as templates to repair the break in an error-free manner and is initiated by extensive nucleolytic processing of the 5′ end of a DSB by DNA end resection (Huertas, 2010; Kass and Jasin, 2010; Symington, 2016). A-NHEJ repair is initiated by limited end resection and involves some of the same factors that comprise the HR end resection machinery (Sfeir and Symington, 2015; Truong et al., 2013). DNA end resection generates 3′ single-stranded DNA (ssDNA), which, if not removed by endonucleases, mitigates the activation of the ataxia-telangiectasia mutated-checkpoint kinase 2 (ATM-CHK2) checkpoint pathway that inhibits C-NHEJ repair (Huertas, 2010; Lieber, 2010). ssDNA overhangs are further sensed and bound by replication protein A (RPA) to recruit ATR interacting protein (ATRIP) and ATR to damage sites (Cortez et al., 2001; Zou and Elledge, 2003). RAD17 loads the RAD9-RAD1-HUS1 (9-1-1) complex to ssDNA to activate ATR-mediated CHK1 phosphorylation, which initiates cell-cycle arrest and DNA repair (Cimprich and Cortez, 2008; Jazayeri et al., 2006; Lee and Dunphy, 2010; Zou et al., 2002). Similar to resected ssDNA, stalled DNA replication forks possess regions of ssDNA that potently activate ATR-CHK1 by coordinating components of the replisome complex, including Claspin, AND-1, Timeless, and Tipin. These factors recruit CHK1 to ssDNA to enable CHK1 activation by ATR so as to maintain genome stability (Chini and Chen, 2003; Hao et al., 2015; Kemp et al., 2010; Kumagai et al., 2004; Lindsey-Boltz et al., 2009).

Another mediator of genome stability is telomeres, repetitive DNA-protein complexes that are protected from inappropriately activating DNA DDR checkpoints by a complex of six core telomere-specific-binding proteins called shelterin (de Lange, 2018). The duplex telomere-binding proteins TRF1 and TRF2-RAP1 and the single-stranded telomere DNA-binding protein POT1

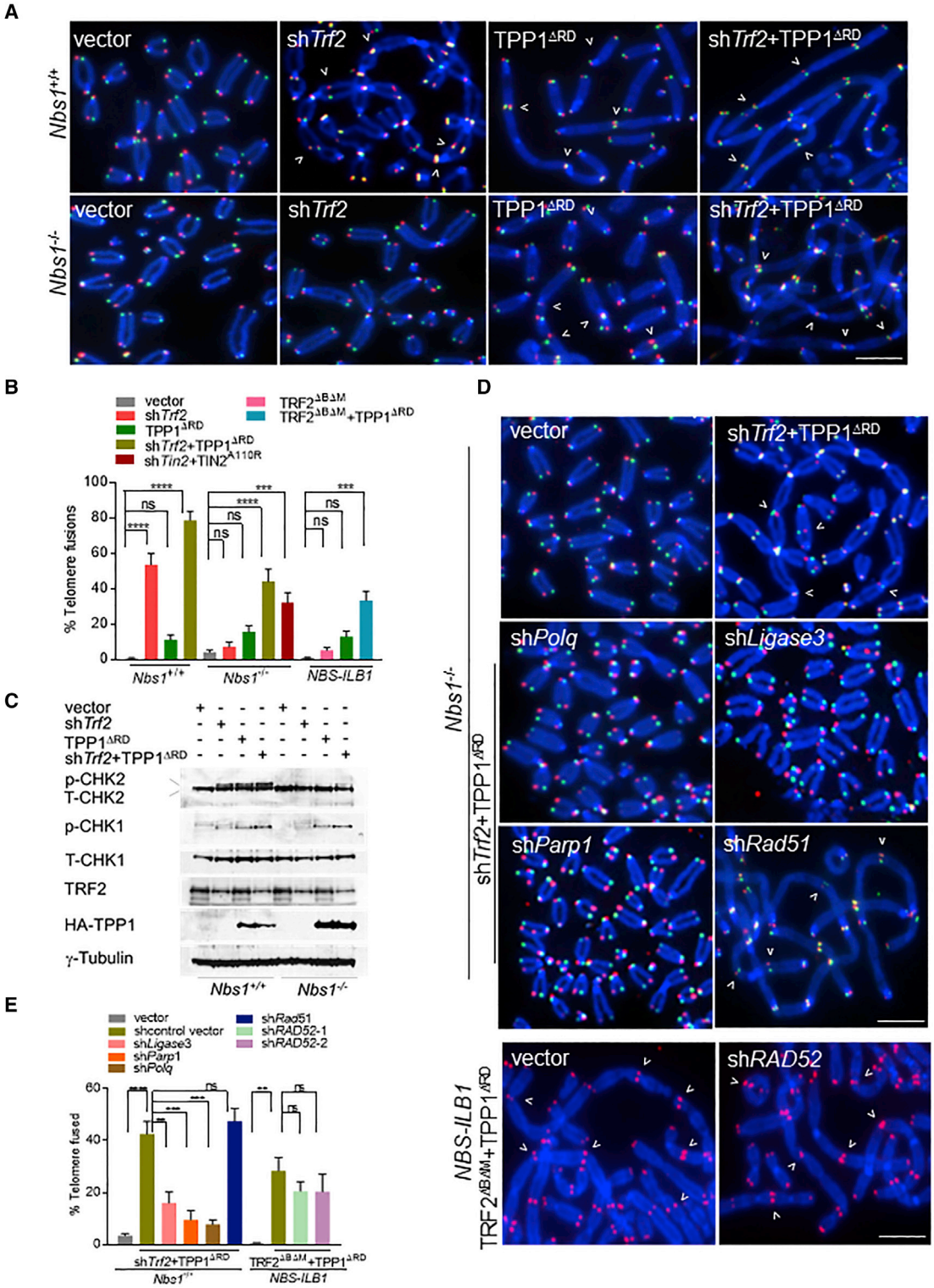

Figure 1. Telomeres Devoid of TRF2 and POT1-TPP1 Are Repaired in an MRN-Independent Manner

(A) *Nbs1*$^{+/+}$ *and Nbs1*$^{-/-}$ MEFs expressing the indicated DNA constructs for 120 h and TelG-FAM (green, leading-strand), TelC-Cy3 (red, lagging-strand), and DAPI (blue) were used to visualize fused chromosomes (arrowheads). Scale bar for all panels: 5 μm.

(B) Telomere fusion frequencies in *NBS-ILB1* cells and in (A). Data are the average of 2 independent experiments ± SD from a minimum of 80 metaphases. ***p = 0.0002, ****p < 0.0001 by 1-way ANOVA. ns, non-significant.

(legend continued on next page)

(POT1a/b in mice) are integral members of this complex. POT1 forms a heterodimer with TPP1, and TIN2 tethers POT1-TPP1 to TRF1 and TRF2 (Wu et al., 2006). The targeted removal of specific shelterin components leads to uncapped chromosome ends that are recognized as DSBs, revealing that unique members of this complex evolved to protect telomeres from engaging in specific DNA repair pathways. In eukaryotes, the MRE11-RAD50-NBS1 (MRN) complex is the primary sensor of DSBs. Deletion of TRF2 in the G1 phase of the cell cycle activates MRN-ATM-CHK2-dependent C-NHEJ-mediated repair (Attwooll et al., 2009; Celli and de Lange, 2005; Deng et al., 2009; Dimitrova and de Lange, 2009). Removal of TRF2 and POT1a/b-TPP1 activates ATR-CHK1-dependent A-NHEJ-mediated repair (Badie et al., 2015; Denchi and de Lange, 2007; Guo et al., 2007; Kibe et al., 2016; Kratz and de Lange, 2018; Rai et al., 2010; Sfeir and de Lange, 2012). In addition, the removal of RAP1 together with the basic domain of TRF2 leads to rapid telomere attrition and formation of end-to-end chromosome fusions due to the activation of HR-mediated repair (Chen et al., 2011; Rai et al., 2016). We recently showed that the interaction of NBS1 with TRF2 dictates the telomere repair pathway choice (Rai et al., 2017). The C-NHEJ-mediated repair of telomeres lacking TRF2 requires phosphorylated NBS1 at serine 432 ($NBS1^{S432}$) to activate ATM, while the interaction of de-phosphorylated $NBS1^{S432}$ with TRF2 promotes the A-NHEJ repair of telomeres lacking POT1a/b-TPP1. In addition, immediately after DNA replication, TRF2 recruits the Apollo/SNM1B nuclease to resect the leading C-strand telomere to generate a short 3′ overhang (Chen et al., 2008; Lam et al., 2010; Rai et al., 2017; Wu et al., 2010). Further resection by EXO1 generates longer overhangs that are inhibitory to NHEJ repair but favor HR (Kibe et al., 2016; Wu et al., 2010, 2012).

Due to their highly repetitive nature and their propensity to adopt aberrant secondary structures, including G-quadruplexes, telomeres represent significant challenges for the replication machinery (Verdun and Karlseder, 2007). TRF1 helps to address this problem by recruiting Timeless, a component of the replisome fork protection complex, to telomeres to prevent replication fork stalling (Leman et al., 2012). However, how the replisome contributes to the repair of damaged DNA is not known. In the present study, we uncover telomere sensing and repair roles engaged by components of the replisome Claspin, Proliferating cell nuclear antigen (PCNA), and Downstream neighbor of SON (DONSON) (CPD). CPD promotes A-NHEJ-mediated repair of dysfunctional telomeres lacking POT1-TPP1 or TRF2-POT1-TPP1 in an MRN- and ATR-ATRIP-independent manner, demonstrating that MRN is not absolutely required for A-NHEJ repair. In the absence of MRN, DNA-PK_{cs} is required to promote CHK1 phosphorylation and A-NHEJ repair. In addition, we show that TRF2 directly interacts with Claspin and, in conjunction with DONSON, promotes the recruitment of EXO1 and CTIP to newly replicated telomeres to mediate C-strand resection and telomere end protection. Our work highlights the contribution of the replisome in mediating the repair of dysfunctional telomeres.

RESULTS

The A-NHEJ Pathway Repairs Telomeres Lacking TRF2 and POT1-TPP1 in an MRN-Independent Manner

We and others have previously shown that C-NHEJ-mediated repair of telomeres devoid of TRF2 requires functional MRN (Attwooll et al., 2009; Deng et al., 2009; Dimitrova and de Lange, 2009). To explore the requirement of the MRN complex in the repair of telomeres lacking shelterin components, we removed POT1a/b-TPP1, TRF2, and POT1a/b-TPP1 or TRF2-TIN2 in WT or *Nbs1* null cell lines. More than 60% of WT mouse embryonic fibroblasts (MEFs) exhibited γ-H2AX or $53BP1^{+}$ dysfunctional telomere-induced foci (TIFs) after the removal of POT1a/b-TPP1 with the dominant negative $TPP1^{\Delta RD}$ allele (Figures S1A and S1B) (Deng et al., 2009; Guo et al., 2007; Hu et al., 2017; Rai et al., 2010, 2011, 2017; Xin et al., 2007). Similar treatment of $Nbs1^{-/-}$ MEFs or human *NBS-ILB1* cells lacking functional NBS1 (Falck et al., 2012; Matsuura et al., 2004) resulted in ~30% of cells displaying TIFs. A similar number of TIFs were observed in both WT and $Nbs1^{-/-}$ MEFs lacking both TRF2 and POT1a/b-TPP1 (Figures S1A and S1B). These results indicate that the DDR is not abrogated at telomeres lacking POT1a/b-TPP1 in the absence of functional MRN.

We next examined the number of telomere fusions in $Nbs1^{-/-}$ MEFs to distinguish between C-NHEJ chromosome fusions stemming from the depletion of TRF2 from A-NHEJ or HR-mediated chromosome fusions stemming from the loss of POT1-TPP1. As expected, only ~6% of telomeres lacking TRF2 were fused in MEFs lacking *Nbs1*. In contrast, the removal of POT1-TPP1 from WT or $Nbs1^{-/-}$ MEFs or *NBS-ILB1* cells generated fusions involving ~15% of all chromosomes, accompanied by robust CHK1 phosphorylation (Figures 1A–1C). In WT MEFs lacking both TRF2 and POT1a/b-TPP1, 80% of all chromosomes were fused, while in $Nbs1^{-/-}$ MEFs or *NBS-ILB1* cells, these fusions decreased to involve ~40% of chromosomes (Figures 1A–1C). Comparable numbers of chromosome fusions (30%–40%) were observed in $Nbs1^{-/-}$ MEFs lacking TRF2-TIN2 (Hu et al., 2017). Similar phenotypes were observed in $Nbs1^{-/-}$ MEFs expressing $TRF2^{\Delta B\Delta M}$ and small hairpin *Tpp1* (sh*Tpp1*) (Figures S1C and S1D). Chromosome orientation-fluorescence *in situ* hybridization (CO-FISH) (Bailey et al., 2001) revealed that chromosomal fusions lacking both TRF2 and POT1a/b-TPP1 took place in G1 phase of the cell cycle, with a small percentage of G2 chromosome and sister chromatid fusions that occurred post-replicatively (Lam et al., 2010) (Figure S1E). These observations indicate that telomeric ends lacking both TRF2 and POT1-TPP1 are

(C) Immunoblot to detect total (T)-CHK1, T-CHK2, phosphorylated (p)-CHK1, and p-CHK2 in $Nbs1^{+/+}$ *and* $Nbs1^{-/-}$ cells expressing indicated proteins. γ-Tubulin, loading control. NS, nonspecific band.

(D) $Nbs1^{-/-}$ MEFs and *NBS-ILB1* cells expressed the indicated DNA constructs for 120 h. TelG-FAM (green), TelC-Cy3 (red), and DAPI (blue) were used to visualize fused chromosomes (arrowheads). Scale bar for all panels: 5 μm.

(E) Telomere fusion frequencies in (D). Data are the average of 3 independent experiments ± SD from a minimum of 120 metaphases. **p = 0.002, ***p = 0.0002, ****p < 0.0001 by 1-way ANOVA. Ns, non-significant.

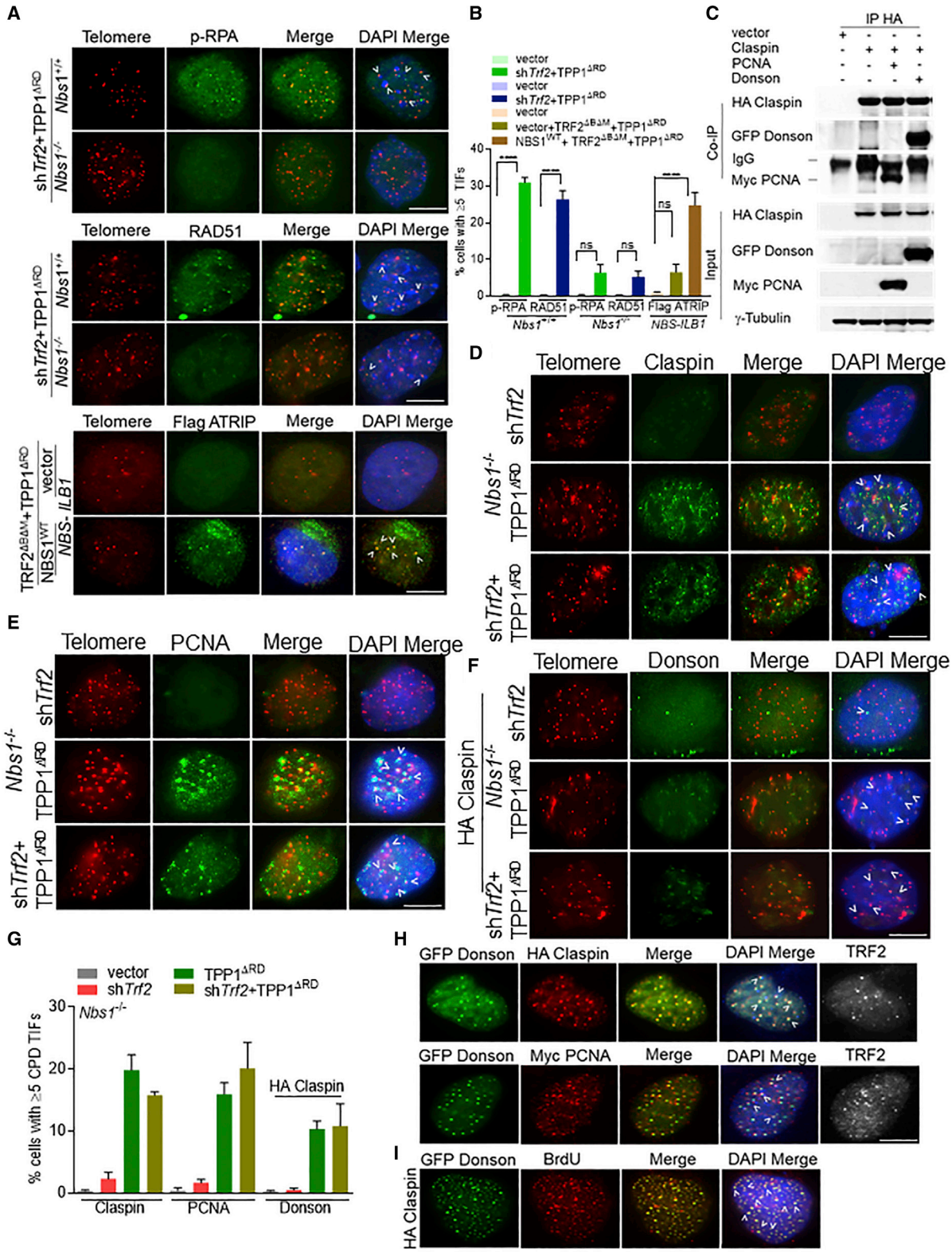

Figure 2. Recruitment of CPD to Telomeres Lacking TRF2 and POT1a/b-TPP1

(A) Co-localization of p-RPA32, RAD51, and Flag-ATRIP with telomeres (arrowheads) in *Nbs1*$^{+/+}$, *Nbs1*$^{-/-}$ MEFs, or *NBS-ILB1* cells. Telomeres were visualized by peptide nucleic acid-fluorescent *in situ* hybridization (PNA-FISH) (red), indicated proteins (green), and nuclei (blue). Scale bar for all panels: 5 μm.

(legend continued on next page)

efficiently repaired in an MRN-independent manner and that this MRN-independent pathway also repairs ~50% of all dysfunctional telomeres lacking both TRF2 and POT1-TPP1 in WT cells. In agreement with previously published results (Yang et al., 2006), treatment of *Nbs1*$^{-/-}$ MEFs with 2 Gy ionizing radiation (IR) also promoted the accumulation of 53BP1 and γ-H2AX to genomic DSBs, accompanied by an increase in the number of genomic chromosomal fusions (Figures S1F–S1H). These results are indicative of a role for MRN-independent repair of both telomeres lacking POT1-TPP1, TRF2, and POT1-TPP1, as well as IR-induced damaged DNA.

We next determined which DNA repair pathways are involved in the MRN-independent repair of telomeres lacking both TRF2 and POT1a/b-TPP1. shRNA-mediated depletion of factors involved in A-NHEJ, including ligase III (Audebert et al., 2004; Rai et al., 2010; Sfeir and de Lange, 2012; Wang et al., 2005), polymerase θ encoded by *Polq* (Ceccaldi et al., 2015; Mateos-Gomez et al., 2015, 2017; Sfeir and de Lange, 2012), and poly (ADP-ribose) polymerase-1 (PARP1) (Audebert et al., 2004; Sfeir and de Lange, 2012), reduced chromosomal fusions by 3- to 5-fold (Figures 1D and 1E). In contrast, the depletion of Rad51 and Rad52, which are known to play an important role in HR and break-induced repair (BIR), respectively (Sotiriou et al., 2016; Verma and Greenberg, 2016), did not appreciably reduce the number of chromosomal fusions (Figures 1D and 1E). We therefore conclude that the repair of dysfunctional telomeres that are devoid of TRF2 and POT1a/b-TPP1 is mediated by MRN-independent A-NHEJ and does not involve C-NHEJ, HR, or BIR pathways.

Replisome Components Claspin, DONSON, and PCNA Localize to Dysfunctional Telomeres Lacking Both TRF2 and POT1-TPP1

We found that the accumulation of ssDNA damage sensor protein RPA at IR-induced DNA damaged foci was reduced by ~80% in the absence of NBS1 (Figure S1F), which supports previously published reports demonstrating that in the absence of functional MRN, RPA localized poorly to damaged ssDNA, preventing the activation of ATR and downstream damage signaling (Jazayeri et al., 2006; Manthey et al., 2007; Stiff et al., 2005; Yuan and Chen, 2010). Similarly, in *Nbs1*$^{-/-}$ MEFs lacking POT1a/b-TPP1 or TRF2 and POT1a/b-TPP1, neither phosphorylated RPA32 (p-RPA32), ATRIP, nor the HR repair protein RAD51 were found to localize to dysfunctional telomeres (Figures 2A, 2B, and S2A). p-RPA32 and ATRIP^{+} TIFs were detected on dysfunctional telomeric ends only after the reconstitution of *NBS-ILB1* cells with WT NBS1 (Figures 2A, 2B, S2B, and S2C). These results further support the observation that in the absence of functional MRN, telomeres lacking both TRF2 and POT1a/b-TPP1 are not repaired by HR. In addition, failure to detect p-RPA32 and ATRIP at these telomeres suggest that ATR is unlikely to be the kinase that phosphorylates CHK1 at these dysfunctional telomeres.

We therefore searched for proteins that mediate both CHK1 activation and DNA repair and identified Claspin, an integral component of the replisome complex (Dungrawala et al., 2015) and an adaptor protein previously shown to mediate CHK1 phosphorylation after DNA damage (Chini and Chen, 2003; Kumagai et al., 2004; Lindsey-Boltz et al., 2009). Using the Fucci system, which uses the fluorescent G1 reporter CDT1 and the S/G2 reporter Geminin (Sakaue-Sawano et al., 2008), we found that Claspin preferentially localizes to the nuclei in S/G2 phases of the cell cycle (Figure S2D) and interacts with a large number of proteins involved in DNA repair and replication (Smits et al., 2019). Co-immunoprecipitation (Co-IP) experiments revealed that Claspin directly interacts with several replisome components, including PCNA and DONSON (Figure 2C) (Reynolds et al., 2017; Yang et al., 2008, 2016). Claspin has been shown to recognize and bind to branched/forked DNA structures containing both double-stranded and ssDNA (Lee et al., 2003; Sar et al., 2004). *In vitro* DNA-binding assays reveal that Claspin binds to a variety of ssDNAs, including telomeric G-rich oligos, telomeric C-rich oligos, and oligo-dT (Figures S2E and S2F). While individual endogenous or epitope-tagged Claspin, PCNA, and DONSON (abbreviated CPD) components localized poorly to dysfunctional telomeres lacking POT1a/b-TPP1 or TRF2 and POT1a/b-TPP1 in WT or *Nbs1*$^{-/-}$ MEFs (Figures 2D–2G, S2G, and S2H), co-expression of any 2 replisome components stabilized complex formation and resulted in a 4-fold increase in CPD localization at both functional and dysfunctional telomeres in U2OS cells (Figures 2H and S2I). shRNA-mediated depletion of any individual CPD component resulted in the instability of the other 2 proteins, suggesting that complex formation promotes CPD stability (Figure S2J). Finally, bromodeoxyuridine (BrdU)-labeling experiments in U2OS cells revealed that CPD readily co-localized with BrdU to newly replicated telomeres (Figures 2I and S2K).

CPD Promotes A-NHEJ-Mediated Repair of Telomeres Lacking Both TRF2 and POT1a/b-TPP1

shRNA-mediated depletion of any of the CPD components individually in WT MEFs lacking both TRF2 and POT1a/b-TPP1 resulted in a ~50% reduction in the number of γ-H2AX^{+} TIFs and end-to-end chromosome fusions observed, revealing that CPD participates in the A-NHEJ-mediated repair of dysfunctional telomeres (Figures 3A and 3B). In both *Nbs1*$^{-/-}$ MEFs and

(B) Percentage of cells containing ≥5 TIFs in (A). Data are the mean of 2 independent experiments ± SD; n > 200 nuclei analyzed per experiment. ****p < 0.0001 by 1-way ANOVA. ns, non-significant.
(C) Co-IP of HA-Claspin with GFP-DONSON or Myc-PCNA in 293T cells. Input, 5% of the total cell lysate. γ-Tubulin, loading control.
(D–F) Localization of Claspin (D), PCNA (E), and DONSON (F) in *Nbs1*$^{-/-}$ MEFs expressing indicated DNAs. Endogenous DONSON TIFs were detectable only in HA-claspin-expressing cells. Telomeres were visualized by PNA-FISH (red), and endogenous CPD was visualized with the indicated antibodies (green). Scale bar for all panels: 5 μm.
(G) Percentage of cells containing ≥5 CPD^{+} foci co-localizing with telomeres, detected in (D)–(F).
(H) Co-expression of HA-Claspin with GFP-DONSON (top panel) or HA-Claspin, Myc-PCNA, and GFP-DONSON (bottom panel) in U2OS cells. Top panel: GFP-DONSON (green) and HA-Claspin (red). Bottom panel: Myc-PCNA (red) and GFP-DONSON (green). For both panels, anti-TRF2 antibody visualized telomeres (white).
(I) HA-Claspin and GFP-DONSON co-localized with BrdU^{+} foci in U2OS cells. GFP-DONSON (green), BrdU (red), and DAPI (blue). Scale bar for all panels: 5 μm.

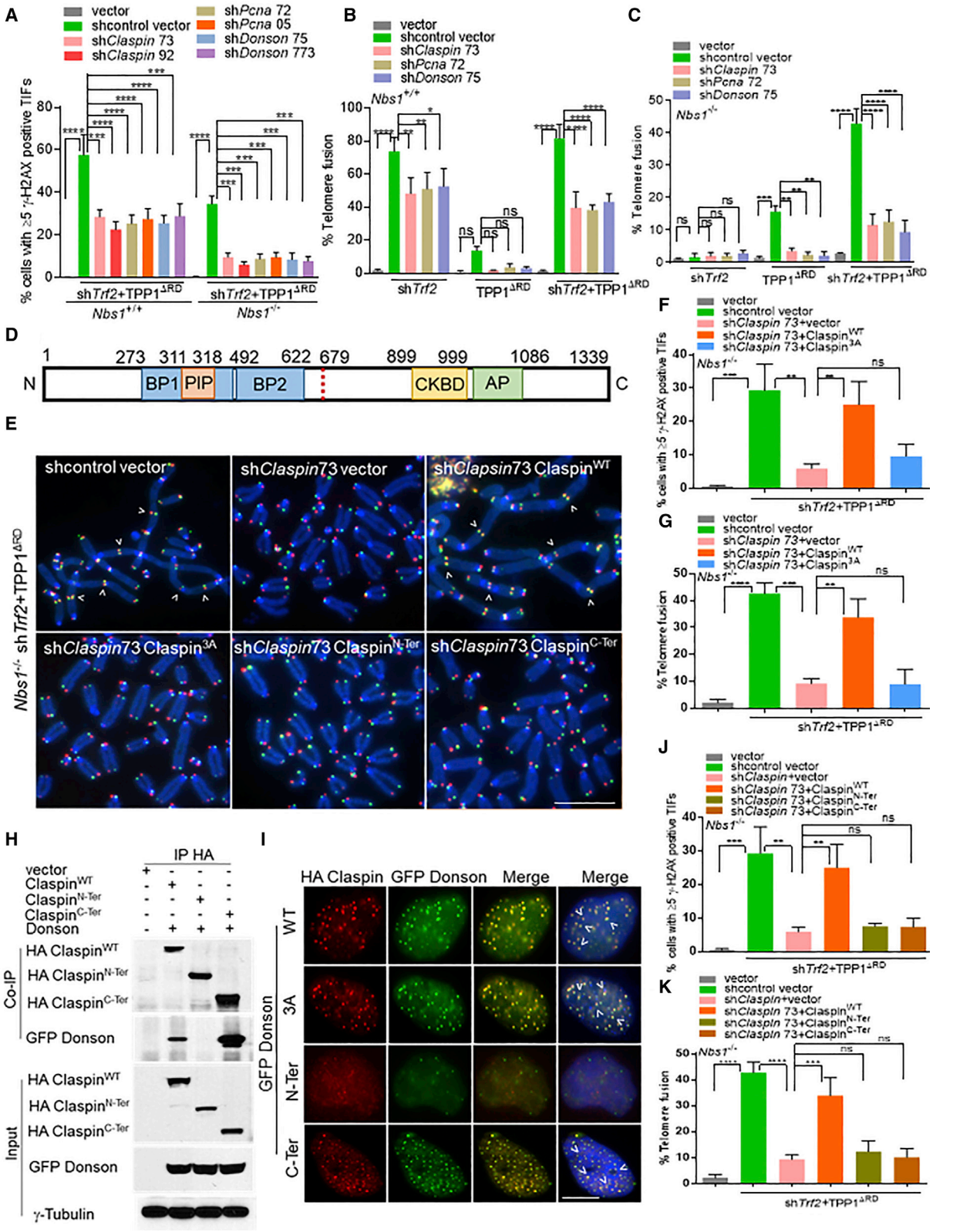

(legend on next page)

NBS-ILB1 cells lacking POT1a/b-TPP1, depleting CPD components individually reduced the number of γ-H2AX or 53BP1^{+} TIFs as well as end-to-end telomere fusions by ~3- to 5-fold without adversely affecting cell-cycle profiles, indicating that CPD plays critical roles in the sensing and repair of these dysfunctional telomeric ends independent of MRN function (Figures 3A–3C and S3A–S3F). CPD also plays a role in the HR-mediated repair of telomeres lacking POT1a/b-TPP1, since Rad51 localization and telomere sister chromatid exchanges (T-SCEs), both hallmarks of HR-mediated repair, were reduced by 3- to 4-fold in the absence of CPD (Figures S3G and S3H). In contrast, CPD is not involved in the C-NHEJ repair of telomeres lacking TRF2 (Figures 3B, 3C, and S3B–S3D).

Claspin contains several functional domains, including a PCNA-interacting protein motif (PIP) near its N terminus and a CHK1-binding domain (CKBD) along with an acidic patch (AP) in its C terminus (Figure 3D) (Smits et al., 2019; Yang et al., 2016). Phosphorylation of the AP by CDC7 prevents the intramolecular interaction of Claspin, promoting its binding to PCNA and DNA substrates (Yang et al., 2016). Three phosphorylation sites in the CKBD domain of Claspin and the mutation of these to alanines (the Claspin^{3A} mutant) abolished the ability of Claspin to promote TIF formation, end-to-end chromosome fusions, and CHK1 phosphorylation (Figures 3E–3G, S3I, S3J, S4A, and S4B) (Lindsey-Boltz et al., 2009). The number of TIFs, chromosome fusions, and CHK1 phosphorylations was almost fully restored when shRNA-resistant WT Claspin but not the Claspin^{3A} mutant was reconstituted into *Nbs1*$^{-/-}$ MEFs lacking TRF2-POT1a/b-TPP1 (Figures 3E–3G, S3I, S3J, S4A, and S4B), revealing that Claspin-mediated CHK1 phosphorylation is essential for the A-NHEJ repair of telomeres lacking POT1a/b-TPP1. We also found that the Claspin N terminus (Claspin$^{N\text{-}Ter}$) interacts with PCNA, while the C terminus (Claspin$^{C\text{-}Ter}$) interacts with DONSON (Figures 3H and S4C). Claspin^{3A} and Claspin$^{C\text{-}Ter}$ but not Claspin$^{N\text{-}Ter}$ are able to co-localize with GFP-DONSON on telomeres, but only Claspin$^{C\text{-}Ter}$ promotes CHK1 phosphorylation (Figures 3I, S4B, and S4D). Depletion of CPD individually abolished TIF formation, chromosome fusion, and CHK1 phosphorylation in *Nbs1*$^{-/-}$ MEFs lacking both TRF2 and POT1a/b/TPP1, and only the expression of WT CPD rescued these phenotypes (Figures 3E–3G, 3J, 3K, S4B, and S4D–S4I). These results suggest that CPD is required for A-NHEJ repair at dysfunctional telomeres lacking both TRF2 and POT1a/b-TPP1 by promoting CHK1 phosphorylation in an MRN-independent manner.

DNA-PK$_{cs}$ Is Required for MRN-Independent CHK1 Phosphorylation

In the absence of functional MRN, telomeres lacking both TRF2 and POT1a/b-TPP1 fail to recruit RPA, ATRIP, and RAD51, suggesting that ATR-ATRIP cannot phosphorylate CHK1 at these telomeres (Figures 2A and 2B). Since expression of the Claspin^{3A} mutant reduced both CHK1 phosphorylation and the A-NHEJ repair of dysfunctional telomeres in *Nbs1*$^{-/-}$ MEFs (Figures 3E–3G and S4B), our data suggest that Claspin-mediated phosphorylation of CHK1 is required for A-NHEJ repair of dysfunctional telomeres in the absence of functional MRN. In support of this observation, Claspin has been shown to participate in ATR-independent phosphorylation of CHK1 (Kumagai et al., 2004; Rodríguez-Bravo et al., 2006). Previous studies also reveal that DNA-dependent protein kinase (DNA-PK$_{cs}$), a key regulator of C-NHEJ repair, is required to maintain Claspin-CHK1 complex stability and is activated by DSBs in the absence of functional MRN (Hartlerode et al., 2015; Lin et al., 2014). We postulated that DNA-PK$_{cs}$ may participate in the phosphorylation of CHK1 at dysfunctional telomeres when MRN function is abrogated. To test this hypothesis, we treated *Nbs1*$^{-/-}$ MEFs bearing dysfunctional telomeres devoid of TRF2 and POT1a/b-TPP1 with the specific DNA-PK$_{cs}$ inhibitor NU7441. The presence of 10 μM of NU7441 decreased both γ-H2AX and 53BP1 TIF formation by 3-fold and resulted in a 4-fold reduction in the number of chromosomal fusions repaired by A-NHEJ (Figures 4A–4D). These levels of TIF and fusion reductions are similar to those observed in cells expressing the Claspin^{3A} mutant. A 4-fold reduction in the level of CHK1 phosphorylation was also

Figure 3. CPD Promotes A-NHEJ-Mediated Chromosome Fusions in the Absence of NBS1

(A) Percentage of cells containing ≥5 γ-H2AX^{+} TIFs in *Nbs1*$^{+/+}$ *and Nbs1*$^{-/-}$ MEFs expressing the indicated DNAs. Data are the mean of 3 independent experiments ± SD; n > 300 nuclei analyzed per experiment. ***p = 0.0002, ****p < 0.0001 by 1-way ANOVA.

(B) Telomere fusion frequencies in *Nbs1*$^{+/+}$ cells treated with sh*Trf2*, TPP1$^{\Delta RD}$, or both. Data are the average of 3 independent experiments ± SD from a minimum of 140 metaphases. *p = 0.01, **p = 0.001, ****p < 0.0001 by 1-way ANOVA. ns, non-significant.

(C) Telomere fusion frequencies in *Nbs1*$^{-/-}$ treated with sh*Trf2*, TPP1$^{\Delta RD}$, or both. Data are the average of 3 independent experiments ± SD from a minimum of 140 metaphases. **p = 0.001, ***p = 0.0001, ****p < 0.0001 by 1-way ANOVA. ns, non-significant.

(D) Domain organization of Claspin. Replication fork-interacting domain, basic patch I, basic patch II, PCNA-interacting domain, CHK1-binding domain, and C-terminal acidic patch. The red dashed line separates Claspin$^{N\text{-}Ter}$ (amino acids [aa] 1–679) and Claspin$^{C\text{-}Ter}$ (aa 679–1,332).

(E) *Nbs1*$^{-/-}$ MEFs expressed the indicated DNA constructs for 120 h. TelG-FAM, TelC-Cy3, and DAPI-labeled metaphase spreads to visualize fused chromosomes (arrowheads). Scale bar for all panels: 5 μm.

(F) Percentage of cells containing ≥5 γ-H2AX TIFs observed in (E). Data are the mean of 2 independent experiments ± SD; n > 200 nuclei analyzed per experiment. **p = 0.01, ***p = 0.001, by 1-way ANOVA. ns, non-significant.

(G) Telomere fusion frequencies in (E). Data are the average of 2 independent experiments ± SD from a minimum of 70 metaphases. **p = 0.001, ***p = 0.0001, ****p < 0.0001 by 1-way ANOVA. ns, non-significant.

(H) Co-IP of HA-Claspin^{WT}, HA-Claspin$^{N\text{-}Ter}$, or HA-Claspin$^{C\text{-}Ter}$ with GFP-DONSON in 293T cells. Input, 5% of the total cell lysate. γ-Tubulin, loading control.

(I) U2OS cells transiently transfected with HA-Claspin^{WT}, HA-Claspin^{3A}, HA-Claspin$^{N\text{-}Ter}$, or HA-Claspin$^{C\text{-}Ter}$ with GFP-DONSON for 48 h. GFP-DONSON (green), HA-Claspin (red), and DAPI to visualize nuclei (blue). Scale bar for all panels: 5 μm.

(J) Percentage of cells containing ≥5 γ-H2AX^{+} TIFs in *Nbs1*$^{-/-}$ MEFs infected with indicated DNA constructs. Data are the mean of 2 independent experiments ± SD; n > 200 nuclei analyzed per experiment. **p = 0.001, ***p = 0.0003 by 1-way ANOVA. ns, non-significant.

(K) Telomere fusion frequencies. Data are the average of 3 independent experiments ± SD from a minimum of 120 metaphases. ***p = 0.001, ****p < 0.0001 by 1-way ANOVA. ns, non-significant.

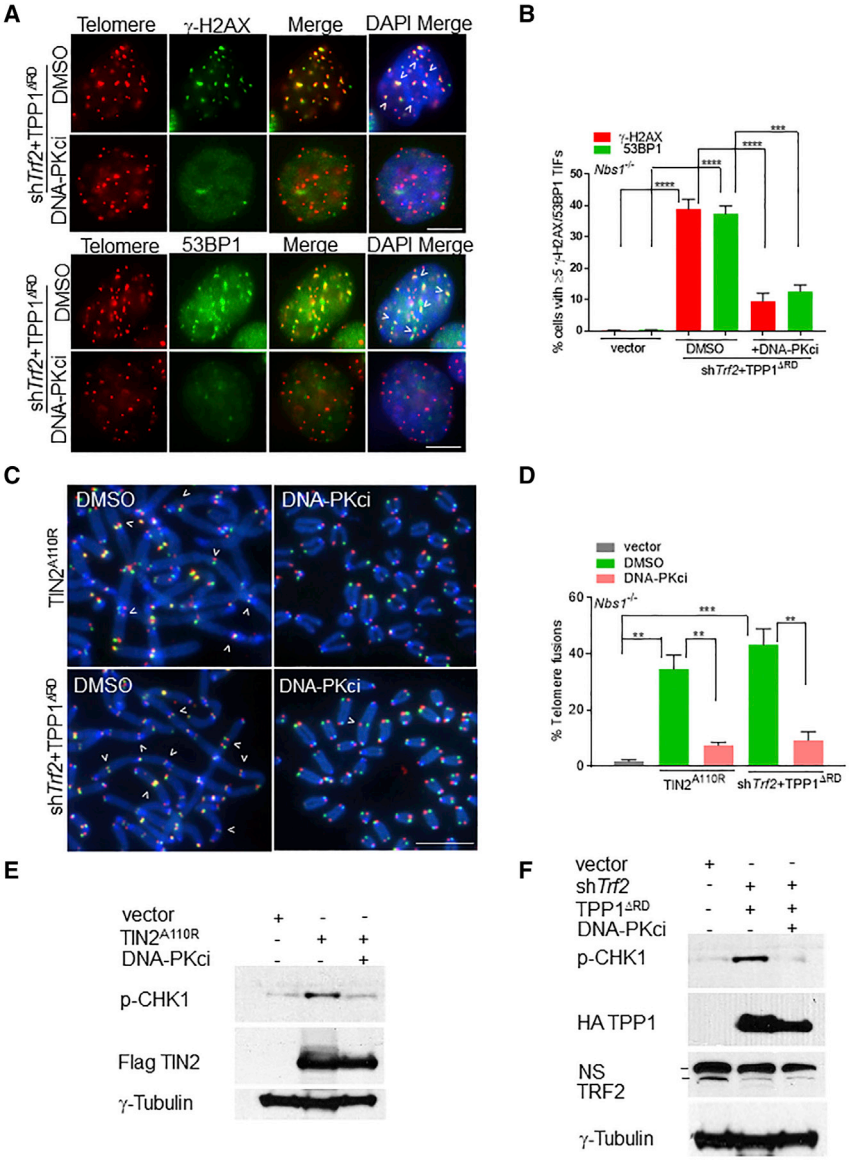

Figure 4. Inhibition of DNA-PK$_{cs}$ Abolishes DDR and A-NHEJ-Mediated Chromosome Fusions in *Nbs1*$^{-/-}$ Cells

(A) *Nbs1*$^{-/-}$ cells expressing the indicated DNA constructs were treated with DMSO or 10 μM DNA-PK$_{cs}$ inhibitor NU7441 and γ-H2AX, and 53BP1^{+} TIFs were detected. Telomeres were visualized by PNA-FISH (red), proteins (green), and nuclei (blue). Scale bar for all panels: 5 μm.

(B) Percentage of cells containing positive γ-H2AX and 53BP1 TIFs in (A). Data are the mean of 2 independent experiments ± SD; n > 200 nuclei analyzed per experiment. ***p = 0.0002, ****p < 0.0001 by 1-way ANOVA.

(C) *Nbs1*$^{-/-}$ MEFs expressing indicated DNA constructs were treated with DMSO or 10 μM NU7441 for 120 h. TelG-FAM, TelC-Cy3, and DAPI were used to visualize fused chromosomes (arrowheads).

(D) Telomere fusion frequencies in (C). Data are the average of 2 independent experiments ± SD from a minimum of 80 metaphases. **p = 0.001, ***p = 0.0005 by 1-way ANOVA. Scale bar for all panels: 5 μm.

(E and F) Immunoblot for p-CHK1 levels in *Nbs1*$^{-/-}$ cells expressing either TIN2^{A110R} (E) or TPP1$^{\Delta RD}$ (F) treated with DMSO or NU7441. γ-tubulin, loading control. NS, nonspecific band.

observed in *Nbs1*$^{-/-}$ MEFs expressing TIN2^{A110R} or TPP1$^{\Delta RD}$ to generate dysfunctional telomeres lacking either TRF2-TIN2 or POT1a/b-TPP1 (Figures 4E and 4F). These data support a critical role for DNA-PK$_{cs}$ to promote efficient CHK1 phosphorylation in MRN-deficient cells bearing dysfunctional telomeres.

CPD Promote DNA End Resection at Telomeres Devoid of TRF2 and POT1a/b-TPP1

Telomeres lacking TRF2-POT1a/b-TPP1 recruit BARD1, CTIP, and BRCA1 in a CPD-dependent manner (Figures 5A and 5B). The shRNA-mediated depletion of CPD decreased the telomeric localization of BARD1 and BRCA1 by ~3-fold (Figures 5C, 5D, S5A, and S5B). These results suggest that BRCA1 and BARD1 play important roles in the repair of telomeres lacking TRF2-POT1a/b-TPP1 in the absence of functional MRN, a notion that is further supported by the observation that the depletion of BRCA1 in *NBS1-ILB1* cells devoid of TRF2-POT1-TPP1 reduced telomere fusions by 3-fold (Figures 5E, 5F, and S5C). We also found that the shRNA-mediated depletion of exonucleases EXO1 and CTIP in *Nbs1*$^{-/-}$ MEFs devoid of TRF2 and POT1a/b-TPP1 reduced end-to-end chromosome fusions by ~4-fold, suggesting that EXO1-mediated nucleolytic processing of the telomeric C-strand is required for A-NHEJ-mediated, MRN-independent repair of dysfunctional telomeres (Figures 5E, 5F, and S5D). To test this notion, we performed telomere restriction fragment (TRF) southern to monitor the length of the G-overhang, which also provides an indication of the amount of C-strand processing. For example, increased C-strand processing would manifest as an increase in the amount of ss telomeric G-strand overhang observed (Gu et al., 2018; Lam et al., 2010). TRF southern of *Nbs1*$^{-/-}$ MEFs devoid of TRF2 and POT1a/b-TPP1 and treated with 2 independent shRNAs targeting either EXO1, CTIP, or CPD individually revealed a reduction in the amount of G-overhang detected, suggesting a defect in C-strand processing (Figures 5G and 5H). To rule out the possibility that this increase in G-overhang elongation is due to telomerase activity, we examined G-overhang formation in telomerase null generation 1 (G1) *mTR*$^{-/-}$ MEFs after removing TRF2 and POT1a/b-TPP1. The lack of telomerase did not abolish the formation of γ-H2AX TIFs, A-NHEJ-mediated end-to-end chromosome fusion, or increased G-overhang formation on these dysfunctional telomeres, ruling out a role for

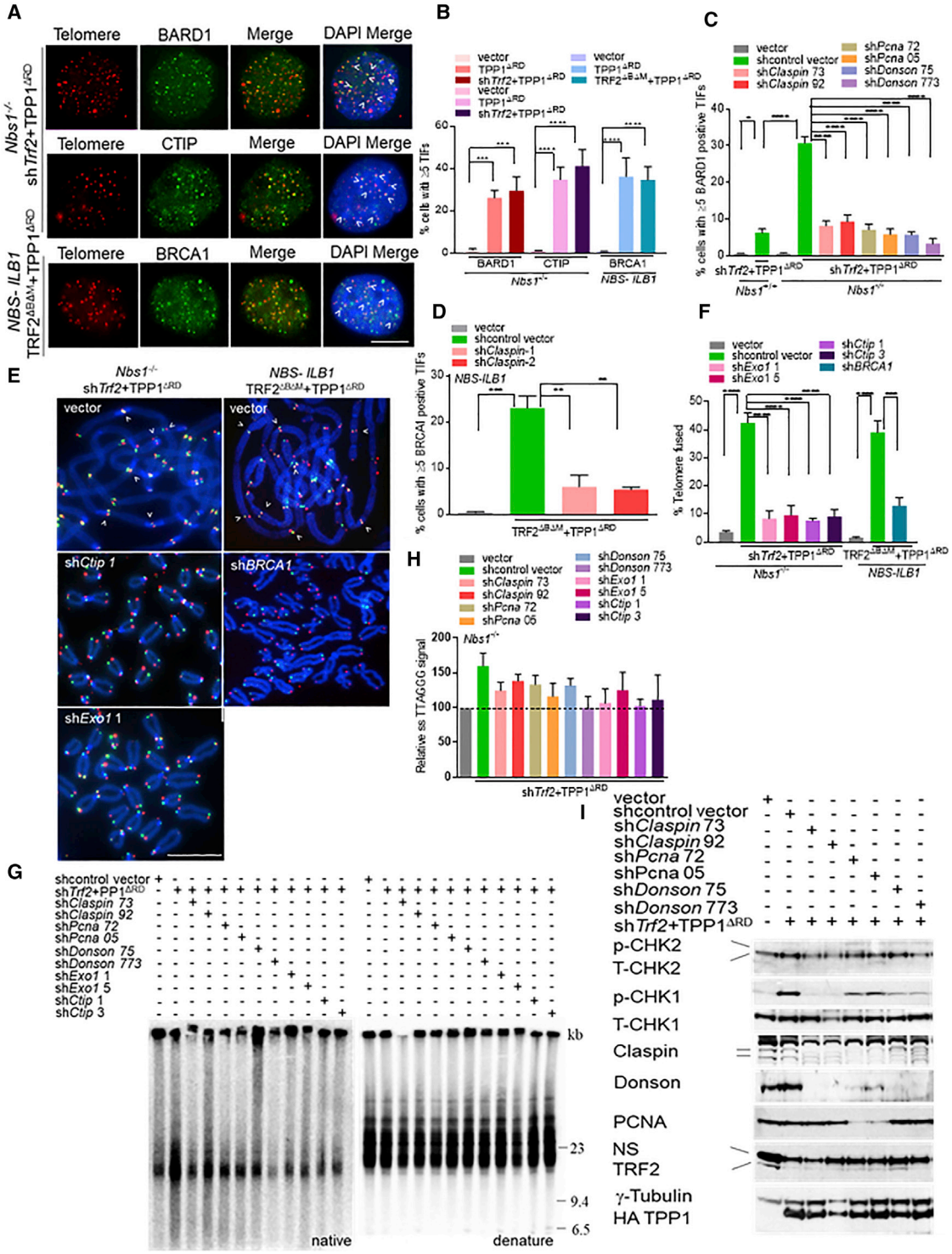

Figure 5. CPD Complex Promotes DNA End Resection at Telomeres Devoid of TRF2 and POT1-TPP1

(A) BARD1, CTIP, and BRCA1 co-localized with telomeres (arrowheads) in *Nbs1*$^{-/-}$ MEFs and *NBS1-ILB1* cells treated with sh*Trf2* and TPP1$^{\Delta RD}$. Telomeres were visualized by PNA-FISH (red), proteins (green), and nuclei (blue). Scale bar for all panels: 5 μm.

(B) Percentage of cells containing ≥5 TIFs in (A). Data represent the mean of 3 independent experiments ± SD; n > 250 nuclei analyzed per experiment. ***p = 0.0001, ****p < 0.0001 by 1-way ANOVA.

(C) Percentage of cells with ≥5 BARD1^{+} TIFs in *Nbs1*$^{+/+}$ or *Nbs1*$^{-/-}$ MEFs treated with the indicated shRNAs and sh*Trf2* + TPP1$^{\Delta RD}$. Data represent the average of 3 independent experiments ± SD; n > 250 nuclei analyzed per experiment. *p = 0.02, ****p < 0.0001 by 1-way ANOVA.

(legend continued on next page)

telomerase in G-overhang elongation (Figures S5E–S5J). The depletion of *Exo1* in G1 *mTR*$^{-/-}$ MEFs resulted in decreased G-overhang formation, further supporting the notion that increased nucleolytic C-strand processing by EXO1 mediates the length of the G-strand at telomeres lacking POT1a/b-TPP1 (Figures S5I and S5J). The shRNA-mediated depletion of CPD, EXO1, and CTIP also resulted in a corresponding decrease in CHK1 phosphorylation in *NBS-ILB1*, *Nbs1*$^{-/-}$, and G1 *mTR*$^{-/-}$ MEFs (Figures 5I, S5D, and S5K). Finally, we addressed the possibility that compromised C-strand fill-in machinery resulted in increased G-overhang. The CTC1-STN1-TEN1 (CST) complex promotes C-strand fill-in with DNA Pol-α, and CST localization to telomeres requires POT1b (Figures S5L and S5M) (Gu et al., 2018; Wu et al., 2012). The expression of TPP1$^{\Delta RD}$ prevents STN1 localization to the 5′ telomeric ends by removing POT1b from telomeres (Figure S5M), compromising the C-strand fill-in machinery. However, even when C-strand fill-in synthesis is inhibited by TPP1$^{\Delta RD}$, the 3′ overhang is still elongated (Figures 5G, 5H, S5I, and S5J). These results suggest that CPD, EXO1, and CTIP are required for the processing of the telomeric C-strand, generating the ss 3′ telomeric overhangs necessary for A-NHEJ-mediated repair.

TRF2 Interacts with Claspin to Recruit CPD and EXO1 to Dysfunctional Telomeres That Resemble Stalled Replication Forks

Telomeric DNA are difficult to replicate regions due to their repetitive nature and propensity to form G4 quadruplexes that can impede the progression of replicative DNA polymerases. POT1 represses the formation of these structures, and its depletion results in replication defects at telomeres (Pinzaru et al., 2016; Rizzo et al., 2009; Zaug et al., 2005). The localization of CPD to telomeres lacking POT1a/b-TPP1 suggests that these dysfunctional telomeres likely adopt difficult-to-repair secondary structures resembling stalled replication forks. Claspin has been shown to recognize and bind to branched/forked DNA structures containing both double-stranded and ssDNA to facilitate phosphorylation of CHK1 by ATR (Lee et al., 2003; Sar et al., 2004). We postulate that CPD is required to help resolve aberrant structures at ss telomeres lacking POT1-TPP1 to promote A-NHEJ repair. To test this hypothesis, we examined the localization of SMARCAL1 (SWI/SNF-related, matrix-associated, actin-dependent regulator of chromatin, subfamily A-like 1), an ATP-dependent annealing helicase that localizes to stalled replication forks to promote replication restart (Bansbach et al., 2009; Cox et al., 2016; Poole et al., 2015; Yusufzai and Kadonaga, 2008). In addition, SMARCAL1 localizes to telomeres undergoing replication stress (Cox et al., 2016). While cells lacking TRF2 displayed only background levels of SMARCAL1^{+} TIFs, 15% of U2OS cells lacking POT1-TPP1 displayed >5 SMARCAL1^{+} TIFs (Figures 6A and S6A). Removal of TRF2 and POT1-TPP1 from telomeres increased the number of cells bearing >5 SMARCAL1^{+} TIFs to 25%. These results suggest that telomeres devoid of POT1-TPP1 adopt secondary structures that recruit CPD and SMARCAL1 to maintain telomere stability. In support of this observation, WT GFP-DONSON readily co-localized with HA-Claspin to telomeres lacking POT1-TPP1 and repressed the telomeric localization of SMARCAL1 to background levels (Figures S6B–S6D).

A recent report identified hypomorphic mutations in DONSON patients that increased the formation of stalled replication forks (Reynolds et al., 2017). DONSON mutants failed to co-localize with HA-Claspin to telomeres lacking POT1-TPP1 and are unable to suppress the telomeric localization of SMARCAL1 (Figures S6B–S6D). These results suggest that telomeres lacking POT1-TPP1 adopted aberrant secondary structures resembling stalled replication forks, leading to the recruitment of SMARCAL1 and CPD. Using immunofluorescence and fluorescence *in situ* hybridization (IF-FISH), we also found that endogenous EXO1 co-localized to dysfunctional telomeres with GFP-DONSON and HA-Claspin (Figures 6B and S6E). Co-immunoprecipitation (Co-IP) experiments revealed that DONSON but not Claspin or PCNA interacts directly with EXO1 and CTIP (Figures 6C and S6F). With the exception of DONSON^{K489T}, all other DONSON mutants examined showed decreased interaction with EXO1 (Tomimatsu et al., 2014), CTIP, and Claspin (Figures 6C, S6G, and S6H).

Following DNA replication, telomeres synthesized from the leading-strand template are blunt ended, while lagging-strand telomeres possess short ssDNA overhangs due to the removal of the terminal Okazaki fragment. Nucleolytic processing of the C-strand by MRE11 and Apollo/SNM1B, followed by more extensive processing by EXO1, generates the 3′ overhang at leading-strand telomeres inhibitory to both leading- and lagging-strand chromatid fusions (Lam et al., 2010; Wu et al., 2012). It is unclear how EXO1 is recruited to newly replicated telomeres. We postulate that the interaction of EXO1 with DONSON (and by extension, CPD) is required for its recruitment to newly replicated telomeres. In support of this notion, sequencing analysis revealed that the C terminus of Claspin possesses a highly evolutionarily conserved TRF2-binding motif (TBM), $_{1286}$Y/F/H-X-L-X-P$_{1290}$ (where X is any amino acid), found

(D) Percentage of cells with ≥5 BRCA1^{+} TIFs in *NBS1-ILB1* cells treated with sh*Claspin 1* or *2* and TRF2$^{\Delta B\Delta M}$ + TPP1$^{\Delta RD}$. Data represent the average of 2 independent experiments ± SD from a minimum of 200 nuclei analyzed per experiment. **p = 0.002, ***p = 0.0008 by 1-way ANOVA. ns, non-significant.
(E) *Nbs1*$^{-/-}$ or *NBS1-ILB1* cells were treated with the indicated DNA constructs for 120 h. TelG-FAM, TelC-Cy3, and DAPI were used to visualize fused chromosomes (arrowheads). Scale bar for all panels: 5 μm.
(F) Telomere fusion frequencies in (E). Data represent the average of 2 independent experiments ± SD from a minimum of 90 metaphases. ***p = 0.0002, ****p < 0.0001 by 1-way ANOVA. ns, non-significant.
(G) Effect of indicated shRNAs on telomere end resection in *Nbs1*$^{-/-}$ MEFs using in-gel hybridization with radiolabeled $(CCCTAA)_4$ probes to detect 3′ ss overhang under native conditions (left) and denaturing conditions to detect total TTAGGG repeats (right).
(H) Quantification of telomeric overhang signals in (G). Single-stranded TTAGGG signals were normalized to the total TTAGGG signal in the same lane and set to 100, and all of the other values are displayed relative to this value.
(I) Immunoblots were examined for the level of indicated proteins in *Nbs1*$^{-/-}$ MEFs expressing indicated DNA constructs and shRNAs targeting CPD. γ-tubulin, loading control. NS, nonspecific band.

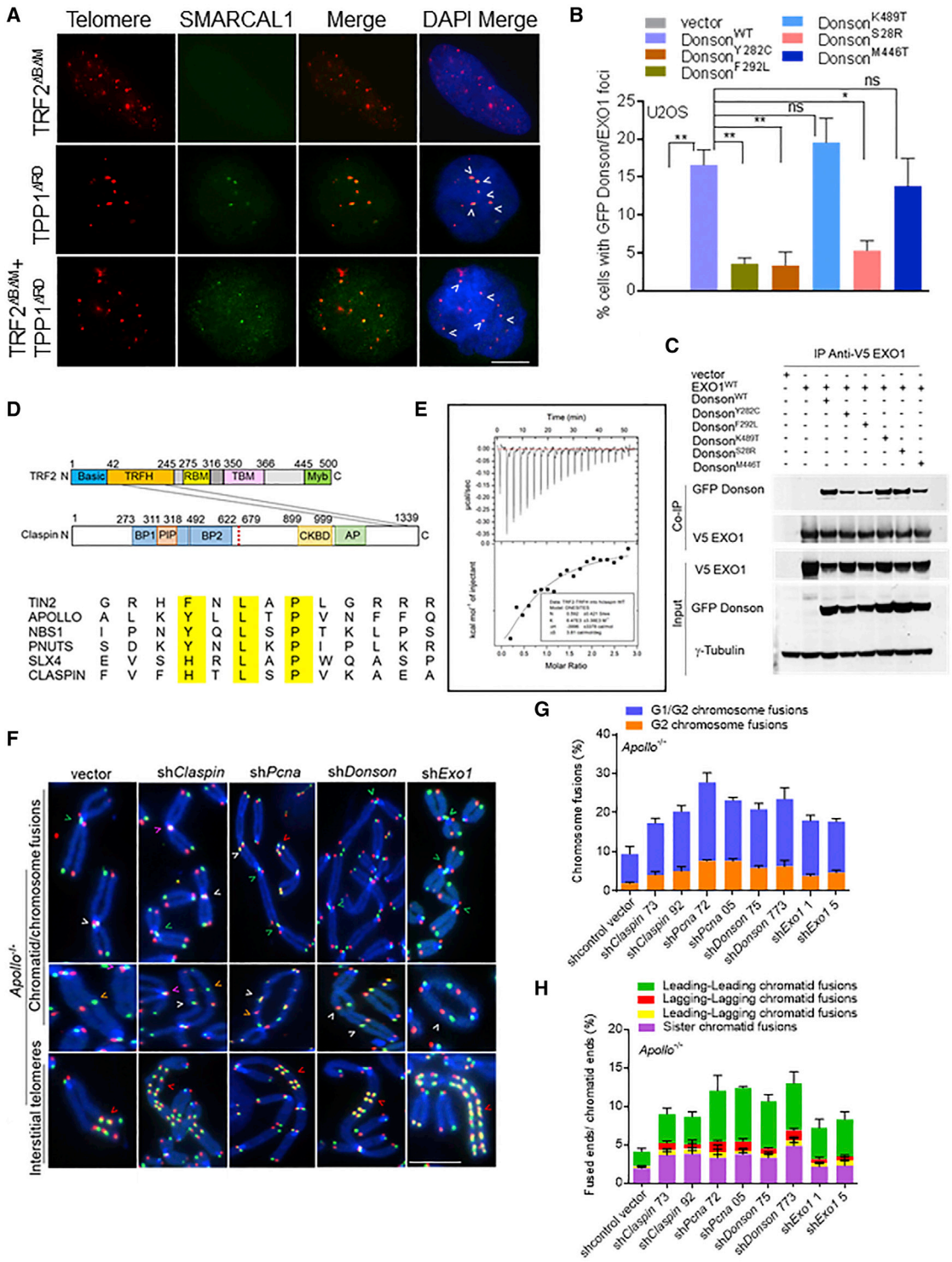

Figure 6. CPD and EXO1 Are Recruited by TRF2 to Dysfunctional Telomeres That Resemble Stalled Replication Forks

(A) SMARCAL1 co-localizes with telomeres in U2OS cells expressing the indicated cDNAs. Telomere PNA-FISH (red), antibody staining (green), and DAPI (blue). Scale bar for all panels: 5 μm.

(B) Co-localization of GFP-DONSON and HA-Claspin with endogenous EXO1 at telomeres. Data represent the mean of 2 independent experiments ± SD; n > 150 nuclei analyzed per experiment. *p = 0.01, **p = 0.001 by 1-way ANOVA. ns, non-significant.

(C) WT GFP-DONSON or mutant DONSON interactions with V5-EXO1. Inputs represent 5% of the total cell lysate used for the IP. γ-tubulin, loading control.

(legend continued on next page)

only in proteins that interact with the TRF2 homology (TRFH) domain (Figures 6D and S6I) (Chen et al., 2008). Isothermal titration calorimetry revealed that the Claspin^{TBM} peptide binds to TRF2^{TRFH} peptide with a K_d of 80 μM (Figure 6E). To further validate TRF2 and Claspin interaction *in vivo*, we performed Co-IP experiments with endogenous proteins in both 293T and *Nbs1*$^{-/-}$ MEFs. Co-IP results revealed that endogenous Claspin interacts with endogenous TRF2, and this interaction was completely abolished by the TRF2^{F120A} mutation, which has been shown to disrupt the ability of the TRF2^{TRFH} domain to interact with TBM-containing proteins (Figures S7A–S7C). These results suggest that the recruitment of Claspin to telomeres occurs via its specific interaction with TRF2.

To characterize the ability of CPD to recruit EXO1 to protect newly replicated telomeres, we used CO-FISH to interrogate *Apollo/SNM1B*$^{-/-}$ MEFs (Lam et al., 2010; Wu et al., 2010). We found that CPD foci readily co-localized to *Apollo/SNM1B*$^{-/-}$ telomeres (Figure S7D). Using CO-FISH to distinguish leading-strand (green signal) and lagging-strand (red signal) telomeres, we found that the deletion of Apollo/SNM1B results in an increase (~5%) in the number of leading-leading-strand chromatid fusions characteristic of post-replicative repair, as well as increased G1/G2 and G2 chromosome fusions following progression through the cell cycle (Figures 6F–6H and S7E) (Lam et al., 2010; Wu et al., 2010). The shRNA-mediated depletion of CPD and EXO1 individually in *Apollo/SNM1B*$^{-/-}$ MEFs resulted in a 2- to 3-fold increase in the number of both leading-strand and lagging-strand chromatid fusions and subsequent G1/G2 and G2 chromosome fusions, suggesting that CPD and EXO1 participate in the C-strand processing of both the leading-ends and the lagging-ends without the need for the enzymatic activity of Apollo/SNM1B to initiate nucleolytic cleavage (Figures 6F–6H and S7F). Expression of the DONSON mutants but not WT DONSON in *Apollo/SNM1B*$^{-/-}$ MEFs increased the number of chromatid and chromosome aberrations, further supporting the notion that these cytogenetic aberrations arise due to defects in telomere replication (Figures S7G and S7H). We also detected a 10-fold increase in the number of chromosomes possessing interstitial telomeric signals (ITSs) of leading-strand and lagging-strand telomeres when CPD or EXO1 was individually depleted in *Apollo/SNM1B*$^{-/-}$ MEFs (Figures 6F and S7I). In addition, the hallmarks of DNA damage, including chromosome breaks, chromosome fragments, radial chromosomes, and fragile telomeres (indicative of telomere replication defects), were also observed when CPD or EXO1 was individually depleted (Figures S7I and S7J). These results suggest that TRF2-mediated recruitment of Apollo/SNM1B, CPD, DONSON, EXO1, and CTIP to newly replicated telomeres is required for nucleolytic processing of the C-strand at both leading and lagging chromosomes. EXO1 and CTIP generates the 3′ overhangs, enabling the loading of POT1-TPP1 to prevent the initiation of A-NHEJ-mediated chromosome and chromatid fusions. Depletion of CPD in an *Apollo/SNM1B*$^{-/-}$ background further compromised G-overhang formation, resulting in the increased cytogenetic aberrations observed.

Mouse Tumors without *Pot1a* Experience Increased Replication Stress

To determine whether the deletion of *Pot1a* promotes replication stress in solid tumors, we examined tumors derived from our *MMTV-Cre*$^{+}$*; Pot1a*$^{F/F}$*; p53*$^{F/F}$ mouse tumor model (Gu et al., 2017). We found that 17/24 of mammary, sarcoma, and salivary tumors generated were genotyped as *Pot1a*$^{F/\Delta}$*; p53*$^{\Delta/\Delta}$, while 7/24 were *Pot1a*$^{\Delta/\Delta}$*; p53*$^{\Delta/\Delta}$ (Figures 7A and S8A; data not shown). Examination of 5 *MMTV-Cre*$^{+}$*; Pot1a*$^{\Delta/\Delta}$*; p53*$^{\Delta/\Delta}$ tumors by western analysis revealed that they were segregated into 2 groups: a Claspin-low group (tumors 4 and 5) and a Claspin-high group (tumors 1–3) (Figure 7A). In the Claspin-low group, p-RPA and p-CHK1 levels were almost undetectable, and γ-H2AX and p-RPA32^{+} TIFs were detected in only 20% of nuclei (Figures 7A, 7D–7F, S8B, and S8C). SMARCAL1^{+} TIFs were also low in these tumors (Figures 7G and S8D), and end-to-end telomere fusions and interstitial telomeres involved only ~1.8% of all chromosome ends (Figures 7H and 7I). In contrast, Claspin-high tumors expressed high levels of p-RPA32, p-CHK1, and SMARCAL1 by western analysis with increase Claspin and PCNA TIFs (Figures 7A–7C). We also detected >5 γ-H2AX^{+} TIFs in 35% of cells and ≥3 p-RPA32^{+} TIFs in 12% of cells, along with increased co-localization of SMARCAL1 on telomeres (Figures 7D–7G and S8B–S8D). Amplification of ITS was found in ~12% of all chromosomes, with tumor number 3 showing such massive ITS amplifications that they can be detected in interphase nuclei (Figures 7H, 7I, and S8B–S8D). Only a small region of the large ITSs contain DSBs that co-localize with γ-H2AX (Figure S8B). These results suggest that the deletion of *Pot1a* results in increased replication stress at telomeres in certain *Pot1a* null tumors, necessitating the increased expression of Claspin and SMARCAL1 to maintain telomere stability. In support of this observation, telomeric replication stress was not detected in *Pot1a*$^{F/\Delta}$*; p53*$^{\Delta/\Delta}$ tumors, since γ-H2AX/p-RPA32^{+} TIFs, interstitial telomeres, and chromosomal aberrations were found at barely detectable levels (Figures 7D–7I and S8B–S8C). Correspondingly, Claspin and SMARCAL1 were undetectable by western analysis (Figure 7A). To further examine the correlation of POT1 and Claspin levels in human cancer, we analyzed the status of Claspin and POT1 gene expression in 308 human colon

(D) (Top) diagram illustrating that the TRF2^{TRFH} domain interacts with the Claspin^{TBM} domain in its C terminus. (Bottom) representative proteins that contain the TBM (F/Y/H-X-L-X-P) are indicated.

(E) ITC measurements of the interaction between TRF2^{TRFH} and Claspin^{TBM} peptides.

(F) Chromosome and chromatid fusions in *Apollo/SNM1B*$^{-/-}$ MEFs treated with indicated shRNAs for 120 h. TelG-FAM, TelC-Cy3, and DAPI were used to visualize fused chromosomes (arrowheads). Representative G1/G2 chromosome fusions (white arrows), G2 chromosome fusions (orange arrows), leading-leading strand (green arrows), sister-sister telomere fusion (pink arrows), and interstitial telomeres (red arrows) are indicated. Scale bar for all panels: 5 μm.

(G) Quantification of G1/G2 and G2 chromosome-type fusions in (F). Data represent the mean of 2 independent experiments ± SD from a minimum of 50 metaphases analyzed per experiment.

(H) Quantification of the chromatid-type and sister fusions in (F). Data represent the mean of 2 independent experiments ± SD from a minimum of 50 metaphases analyzed per experiment.

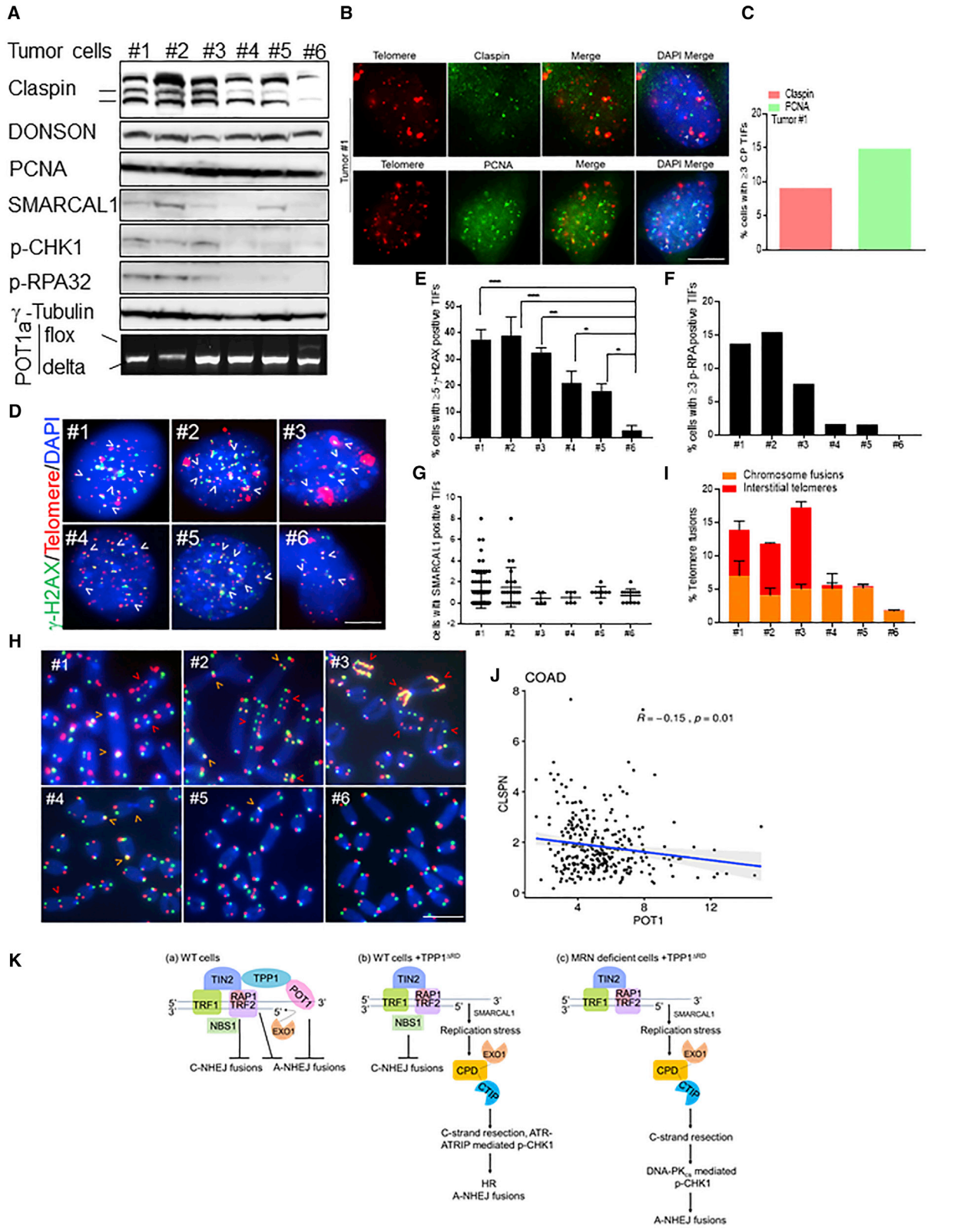

(legend on next page)

carcinomas in The Cancer Genome Atlas (TCGA) database. We found a significant negative correlation between POT1 and Claspin gene expression in these cancers (Figure 7J).

DISCUSSION

In this study, we describe unexpected roles for the replisome components Claspin, PCNA, and DONSON at telomeres. CPD is recruited to telomeres through the interaction of Claspin with TRF2-RAP1, while DONSON interacts with EXO1 and CTIP. Together, these proteins promote telomeric C-strand resection and the generation of 3′ G-overhangs, which serve as a platform for POT1-TPP1 binding to protect telomeres from initiating A-NHEJ repair (Figure 7Ka). Dysfunctional telomeres lacking POT1-TPP1 also generate aberrant secondary structures that are inhibitory to A-NHEJ repair, requiring resolution by CPD and SMARCAL (Figure 7Kb). In the absence of functional MRN, Claspin-mediated CHK1 phosphorylation and A-NHEJ repair requires DNA-PK$_{cs}$ (Figure 7Kc). Finally, mouse tumors lacking Pot1a display increased telomere replication stress (RS) and elevated Claspin expression. Our results highlight the importance of CPD in promoting the A-NHEJ repair of dysfunctional telomeres lacking POT1-TPP1.

Role of Replisome Components in the Repair of Telomeres Lacking POT1-TPP1 by A-NHEJ

Telomere DNA is difficult to replicate due to its highly repetitive nature and ability to form aberrant secondary structures that impede polymerase progression (Crabbe et al., 2004; Gilson and Géli, 2007; Rizzo et al., 2009; Zaug et al., 2005). TRF1 promotes normal fork progression through telomeres by recruiting the helicases RTEL1 and BLM to facilitate lagging-strand telomere synthesis by resolving G4 quadruplexes (Sfeir et al., 2009; Vannier et al., 2012, 2013). The interaction of RTEL1 with PCNA is essential for proper telomere replication. Our findings also highlight a role for the replisome in mediating the repair of dysfunctional telomeres. Telomeres devoid of POT1-TPP1 activate ATR-dependent hyper-resection of the 5′ C-strand, resulting in the generation of long 3′ ss overhangs (Kibe et al., 2016). Since POT1-TPP1 functions to repress RPA from loading onto 3′ G-overhangs (Flynn et al., 2011; Gong and de Lange, 2010), we postulate that in the absence of POT1-TPP1, telomeres adopt aberrant secondary DNA structures similar to those found in stalled replication forks. Claspin specifically interacts with TRF2 to help resolve these structures and facilitate A-NHEJ repair independent of MRN status. In support of this notion, shRNA-mediated depletion of individual CPD components reduced A-NHEJ-mediated chromosome fusions to levels similar to those observed when Pol-θ, PARP1, or ligase III are removed, indicative of their importance to promote the A-NHEJ repair of ss telomeric ends. Our data also suggest that CTIP, BRCA1, and EXO1 play roles in mediating the extensive 5′-3′ C-strand resection necessary to generate the long tracks of microhomologies necessary for A-NHEJ repair in the absence of TRF2-POT1-TPP1. Furthermore, localization of RPA to ssDNA represses Pol-θ-mediated A-NHEJ repair and instead channels the ssDNA substrates for HR-mediated repair (Mateos-Gomez et al., 2017). Since telomeres lacking POT1-TPP1 cannot recruit RPA in the absence of MRN, they must be repaired through A-NHEJ.

While ITC revealed that the interaction between Claspin^{TBM} and TRF2^{TRFH} peptides is relatively weak, it is important to note that the ability of Claspin to localize to telomeres increases when both PCNA and DONSON are present (Figures 2H and S2I), suggesting that the interaction of the CPD complex with TRF2 is likely substantially stronger than *in vitro* peptide interactions.

DNA-PK$_{cs}$-Dependent, MRN-Independent Phosphorylation of CHK1 for A-NHEJ Repair

In the absence of the functional MRN complex, RPA localized poorly to damaged ssDNA, preventing the activation of ATR-ATRIP and downstream damage signaling through CHK1 (Jazayeri et al., 2006; Manthey et al., 2007; Stiff et al., 2005; Yuan and Chen, 2010). However, NBS1 has been shown to directly activate ATR independently of MRE11 and TOPBP1 function (Kobayashi et al., 2013). The *Ustilago maydis* Claspin homolog Mrc1 but not MRN is required to initiate the CHK1-dependent DNA damage response necessary for cell-cycle arrest (Tenorio-Gómez et al., 2015). This result suggests that MRN activation of the ATR/CHK1 pathway is dispensable under certain DNA damage conditions, and that Claspin could substitute for MRN function. In the absence of functional MRN, RPA and ATRIP fail to localize to telomeres lacking POT1-TPP1,

Figure 7. Genomic Instability in Tumors Derived from MMTV-Cre; *p53$^{F/F}$*; *Pot1a$^{F/F}$* Mice

(A) CPD, SMARCAL1, p-CHK1, and p-RPA32 expression in MMTV-Cre; *p53$^{\Delta/\Delta}$*; *Pot1a$^{\Delta/\Delta}$* breast tumors (#1, 3, and 4), sarcoma (#2), and salivary gland tumor (#5). Tumor #6 is MMTV-Cre; *p53$^{\Delta/\Delta}$*; *Pot1a$^{F/\Delta\Delta}$*. γ-Tubulin, loading control. Bottom panel: PCR genotyping.

(B) Detection of Claspin and PCNA (green) and telomeres (red) in tumor #1.

(C) Percentage of cells containing ≥3 Claspin/PCNA (CP^{+}) TIFs in (B). Scale bar for all panels: 5 μm.

(D) γ-H2AX TIFs in tumor cell lines. Telomere PNA-FISH (red), antibody staining (green), and nuclei (blue). Scale bar for all panels: 5 μm.

(E) Percentage of cells containing ≥5 γ-H2AX TIFs in (D). Data represent the mean of 2 independent experiments ± SD; n > 200 nuclei analyzed per experiment. *p = 0.01, **p = 0.001, ***p = 0.0001 by 1-way ANOVA.

(F) Percentage of cells containing ≥3 p-RPA32 TIFs in tumor cell lines.

(G) SMARCAL1 TIFs in tumor cell lines.

(H) Interstitial telomeres (red arrow), chromosome and sister chromatid fusions (orange arrow) in *Pot1a* deleted mouse tumor cell lines. TelG-FAM, TelC-Cy3, and DAPI were used to visualize fused chromosomes. Scale bar for all panels: 5 μm.

(I) Quantification of the number of interstitial telomeres and chromosome fusions in (H). Data represent the average of 2 independent experiments ± SD from a minimum of 70 metaphases.

(J) Spearman's correlation between claspin and POT1 gene expression in colon adenocarcinoma obtained from TCGA data.

(K) Schematic depicting CPD functions. See text for details.

suggesting that the MRN-ATRIP-ATR cascade required for CHK1 phosphorylation is dispensable for A-NHEJ repair. We now show that DNA-PK$_{cs}$ can substitute for MRN function by promoting CHK1 phosphorylation and A-NHEJ-mediated repair at telomeres lacking POT1-TPP1, an observation that is in line with a previous report suggesting that DNA-PK$_{cs}$ is required to maintain Claspin-CHK1 complex stability (Lin et al., 2014).

CTIP Functions Independently of MRN for A-NHEJ Repair of Dysfunctional Telomeres Lacking POT1a/b-TPP1

In mammalian cells, MRE11-CTIP nucleases are required to resect DSBs to generate the resected 3′ overhangs necessary for annealing and A-NHEJ repair (Buis et al., 2012; Dinkelmann et al., 2009; Rass et al., 2009; Xie et al., 2009). While MRN-CTIP is essential for C-NHEJ-mediated repair of telomeres lacking TRF2 (Attwooll et al., 2009; Deng et al., 2009; Dinkelmann et al., 2009), our data indicate that MRN but not CTIP is dispensable for A-NHEJ-mediated repair of telomeres lacking POT1a/b-TPP1. While CTIP has been shown to enhance the nuclease activity of MRE11 to promote A-NHEJ repair (Badie et al., 2015; Bennardo et al., 2008; Kibe et al., 2016; Lee-Theilen et al., 2011; Rass et al., 2009; Sfeir and de Lange, 2012; Xie et al., 2009; Zhang and Jasin, 2011), CTIP nuclease activity independent of MRN function has also been reported (Lee-Theilen et al., 2011). Our data strongly suggest that at least at telomeres lacking POT1a/b-TPP1, CTIP is required to promote A-NHEJ-mediated repair in the absence of the functional MRN complex, a notion that is consistent with the MRN-independent nuclease activity of CTIP/Sae2 (Lengsfeld et al., 2007; Makharashvili et al., 2014; Przetocka et al., 2018; Wang et al., 2014; Yu et al., 2018).

POT1 Protects Tumors from Replication Stress

At stalled replication forks, RPA serves as a platform to recruit fork repair proteins to promote fork restart and restore replication (Bhat and Cortez, 2018). After fork restart, RPA must be displaced for DNA replication to proceed normally. POT1 has been shown to participate in RPA exclusion at telomeres (Flynn et al., 2011). We postulate that POT1 may serve an analogous function at telomere replication forks. The deletion of POT1 is thus expected to result in increased replicative stress at telomeres. A subset of *MMTV-Cre; Pot1a*$^{\Delta/\Delta}$*; p53*$^{\Delta/\Delta}$ tumors show high levels of Claspin expression, elevated p-CHK1 levels, and increased localization of γ-H2AX and SMARCAL1 to telomeres, all indicative of increased telomere replication stress. Our data suggest that the upregulation of Claspin is required to maintain genome stability in tumors with high levels of RS. In support of this notion, a recent report demonstrates that the increased expression of Claspin, Timeless, and CHK1 is observed in a diverse array of primary human tumors to enable tolerance to increased RS and maintain the integrity of the replication fork (Bianco et al., 2019).

STAR★METHODS

Detailed methods are provided in the online version of this paper and include the following:

- KEY RESOURCES TABLE
- LEAD CONTACT AND MATERIALS AVAILABILITY
- EXPERIMENTAL MODEL AND SUBJECT DETAILS
  - Cell lines
  - Mouse tumor model for generation of MMTV-Cre; mPot1a$^{F/F}$; p53$^{F/F}$ tumor cell lines
- METHOD DETAILS
  - Retroviral infection
  - Western blot analysis
  - Immunofluorescence and fluorescent *in situ* hybridization
  - Coimmunoprecipitation
  - Isothermal titration calorimetry
  - DNA binding assay
  - Cell Cycle analysis
  - Chromosome analysis by telomere PNA-FISH and CO-FISH
  - Telomere length analysis and G-Strand overhang assays
- QUANTIFICATION AND STATISTICAL ANALYSIS
- DATA AND CODE AVAILABILITY

SUPPLEMENTAL INFORMATION

Supplemental Information can be found online at https://doi.org/10.1016/j.celrep.2019.11.012.

ACKNOWLEDGMENTS

We thank the members of the Chang lab for helpful suggestions. We thank Dr. Lee Zou and Dr. Kenshi Komatsu for kindly providing *Nbs1*$^{-/-}$ MEFs, Dr. Steve Jackson for human *NBS-ILB1* cells, Dr. Grant S. Stewart for DONSON constructs, Dr. Sandeep Verma for EXO1 cDNA constructs, Dr. Lesley Devine for performing flow cytometry, and Yuping Zhang for analyzing Claspin and POT1 gene expression. This work was supported by the National Cancer Institute, United States (RO1 CA129037 and RO1 CA202816 to S.C.).

AUTHOR CONTRIBUTIONS

R.R. and S.C. conceived the project and designed the experiments. R.R. performed the biochemistry and molecular biology experiments. C.B. performed the molecular cloning and immunofluorescence microscopy. P.G. generated the tumor mouse model and analyzed the tumor cell lines. Y.C. performed the ITC experiments. C.K.-S. analyzed POT1 and Claspin gene expression using TCGA database. R.R., P.G., C.B., and Y.C. generated the data for the figures. R.R., P.G., and S.C. analyzed and interpreted the data, composed the figures, and wrote the paper.

DECLARATION OF INTERESTS

The authors declare no competing interests.

Received: April 5, 2019
Revised: September 22, 2019
Accepted: November 4, 2019
Published: December 10, 2019

REFERENCES

Aguilera, A., and Gómez-González, B. (2008). Genome instability: a mechanistic view of its causes and consequences. Nat. Rev. Genet. *9*, 204–217.

Attwooll, C.L., Akpinar, M., and Petrini, J.H. (2009). The mre11 complex and the response to dysfunctional telomeres. Mol. Cell. Biol. *29*, 5540–5551.

Audebert, M., Salles, B., and Calsou, P. (2004). Involvement of poly(ADP-ribose) polymerase-1 and XRCC1/DNA ligase III in an alternative route for DNA double-strand breaks rejoining. J. Biol. Chem. *279*, 55117–55126.

Badie, S., Carlos, A.R., Folio, C., Okamoto, K., Bouwman, P., Jonkers, J., and Tarsounas, M. (2015). BRCA1 and CtIP promote alternative non-homologous end-joining at uncapped telomeres. EMBO J. *34*, 828.

Bailey, S.M., Cornforth, M.N., Kurimasa, A., Chen, D.J., and Goodwin, E.H. (2001). Strand-specific postreplicative processing of mammalian telomeres. Science *293*, 2462–2465.

Bansbach, C.E., Bétous, R., Lovejoy, C.A., Glick, G.G., and Cortez, D. (2009). The annealing helicase SMARCAL1 maintains genome integrity at stalled replication forks. Genes Dev. *23*, 2405–2414.

Bennardo, N., Cheng, A., Huang, N., and Stark, J.M. (2008). Alternative-NHEJ is a mechanistically distinct pathway of mammalian chromosome break repair. PLoS Genet. *4*, e1000110.

Bhat, K.P., and Cortez, D. (2018). RPA and RAD51: fork reversal, fork protection, and genome stability. Nat. Struct. Mol. Biol. *25*, 446–453.

Bianco, J.N., Bergoglio, V., Lin, Y.L., Pillaire, M.J., Schmitz, A.L., Gilhodes, J., Lusque, A., Mazières, J., Lacroix-Triki, M., Roumeliotis, T.I., et al. (2019). Overexpression of Claspin and Timeless protects cancer cells from replication stress in a checkpoint-independent manner. Nat. Commun. *10*, 910.

Buis, J., Stoneham, T., Spehalski, E., and Ferguson, D.O. (2012). Mre11 regulates CtIP-dependent double-strand break repair by interaction with CDK2. Nat. Struct. Mol. Biol. *19*, 246–252.

Ceccaldi, R., Liu, J.C., Amunugama, R., Hajdu, I., Primack, B., Petalcorin, M.I., O'Connor, K.W., Konstantinopoulos, P.A., Elledge, S.J., Boulton, S.J., et al. (2015). Homologous-recombination-deficient tumours are dependent on Polθ-mediated repair. Nature *518*, 258–262.

Celli, G.B., and de Lange, T. (2005). DNA processing is not required for ATM-mediated telomere damage response after TRF2 deletion. Nat. Cell Biol. *7*, 712–718.

Chen, Y., Yang, Y., van Overbeek, M., Donigian, J.R., Baciu, P., de Lange, T., and Lei, M. (2008). A shared docking motif in TRF1 and TRF2 used for differential recruitment of telomeric proteins. Science *319*, 1092–1096.

Chen, Y., Rai, R., Zhou, Z.R., Kanoh, J., Ribeyre, C., Yang, Y., Zheng, H., Damay, P., Wang, F., Tsujii, H., et al. (2011). A conserved motif within RAP1 has diversified roles in telomere protection and regulation in different organisms. Nat. Struct. Mol. Biol. *18*, 213–221.

Chini, C.C., and Chen, J. (2003). Human claspin is required for replication checkpoint control. J. Biol. Chem. *278*, 30057–30062.

Ciccia, A., and Elledge, S.J. (2010). The DNA damage response: making it safe to play with knives. Mol. Cell *40*, 179–204.

Cimprich, K.A., and Cortez, D. (2008). ATR: an essential regulator of genome integrity. Nat. Rev. Mol. Cell Biol. *9*, 616–627.

Cortez, D., Guntuku, S., Qin, J., and Elledge, S.J. (2001). ATR and ATRIP: partners in checkpoint signaling. Science *294*, 1713–1716.

Cox, K.E., Maréchal, A., and Flynn, R.L. (2016). SMARCAL1 Resolves Replication Stress at ALT Telomeres. Cell Rep. *14*, 1032–1040.

Crabbe, L., Verdun, R.E., Haggblom, C.I., and Karlseder, J. (2004). Defective telomere lagging strand synthesis in cells lacking WRN helicase activity. Science *306*, 1951–1953.

de Lange, T. (2018). Shelterin-Mediated Telomere Protection. Annu. Rev. Genet. *52*, 223–247.

Denchi, E.L., and de Lange, T. (2007). Protection of telomeres through independent control of ATM and ATR by TRF2 and POT1. Nature *448*, 1068–1071.

Deng, Y., Guo, X., Ferguson, D.O., and Chang, S. (2009). Multiple roles for MRE11 at uncapped telomeres. Nature *460*, 914–918.

Dimitrova, N., and de Lange, T. (2009). Cell cycle-dependent role of MRN at dysfunctional telomeres: ATM signaling-dependent induction of nonhomologous end joining (NHEJ) in G1 and resection-mediated inhibition of NHEJ in G2. Mol. Cell. Biol. *29*, 5552–5563.

Dinkelmann, M., Spehalski, E., Stoneham, T., Buis, J., Wu, Y., Sekiguchi, J.M., and Ferguson, D.O. (2009). Multiple functions of MRN in end-joining pathways during isotype class switching. Nat. Struct. Mol. Biol. *16*, 808–813.

Dungrawala, H., Rose, K.L., Bhat, K.P., Mohni, K.N., Glick, G.G., Couch, F.B., and Cortez, D. (2015). The Replication Checkpoint Prevents Two Types of Fork Collapse without Regulating Replisome Stability. Mol. Cell *59*, 998–1010.

Falck, J., Forment, J.V., Coates, J., Mistrik, M., Lukas, J., Bartek, J., and Jackson, S.P. (2012). CDK targeting of NBS1 promotes DNA-end resection, replication restart and homologous recombination. EMBO Rep. *13*, 561–568.

Flynn, R.L., Centore, R.C., O'Sullivan, R.J., Rai, R., Tse, A., Songyang, Z., Chang, S., Karlseder, J., and Zou, L. (2011). TERRA and hnRNPA1 orchestrate an RPA-to-POT1 switch on telomeric single-stranded DNA. Nature *471*, 532–536.

Gilson, E., and Géli, V. (2007). How telomeres are replicated. Nat. Rev. Mol. Cell Biol. *8*, 825–838.

Gong, Y., and de Lange, T. (2010). A Shld1-controlled POT1a provides support for repression of ATR signaling at telomeres through RPA exclusion. Mol. Cell *40*, 377–387.

Gu, P., Wang, Y., Bisht, K.K., Wu, L., Kukova, L., Smith, E.M., Xiao, Y., Bailey, S.M., Lei, M., Nandakumar, J., and Chang, S. (2017). Pot1 OB-fold mutations unleash telomere instability to initiate tumorigenesis. Oncogene *36*, 1939–1951.

Gu, P., Jia, S., Takasugi, T., Smith, E., Nandakumar, J., Hendrickson, E., and Chang, S. (2018). CTC1-STN1 coordinates G- and C-strand synthesis to regulate telomere length. Aging Cell *17*, e12783.

Guo, X., Deng, Y., Lin, Y., Cosme-Blanco, W., Chan, S., He, H., Yuan, G., Brown, E.J., and Chang, S. (2007). Dysfunctional telomeres activate an ATM-ATR-dependent DNA damage response to suppress tumorigenesis. EMBO J. *26*, 4709–4719.

Hao, J., de Renty, C., Li, Y., Xiao, H., Kemp, M.G., Han, Z., DePamphilis, M.L., and Zhu, W. (2015). And-1 coordinates with Claspin for efficient Chk1 activation in response to replication stress. EMBO J. *34*, 2096–2110.

Hartlerode, A.J., Morgan, M.J., Wu, Y., Buis, J., and Ferguson, D.O. (2015). Recruitment and activation of the ATM kinase in the absence of DNA-damage sensors. Nat. Struct. Mol. Biol. *22*, 736–743.

Hu, C., Rai, R., Huang, C., Broton, C., Long, J., Xu, Y., Xue, J., Lei, M., Chang, S., and Chen, Y. (2017). Structural and functional analyses of the mammalian TIN2-TPP1-TRF2 telomeric complex. Cell Res. *27*, 1485–1502.

Huertas, P. (2010). DNA resection in eukaryotes: deciding how to fix the break. Nat. Struct. Mol. Biol. *17*, 11–16.

Jackson, S.P., and Bartek, J. (2009). The DNA-damage response in human biology and disease. Nature *461*, 1071–1078.

Jazayeri, A., Falck, J., Lukas, C., Bartek, J., Smith, G.C., Lukas, J., and Jackson, S.P. (2006). ATM- and cell cycle-dependent regulation of ATR in response to DNA double-strand breaks. Nat. Cell Biol. *8*, 37–45.

Kass, E.M., and Jasin, M. (2010). Collaboration and competition between DNA double-strand break repair pathways. FEBS Lett. *584*, 3703–3708.

Kemp, M.G., Akan, Z., Yilmaz, S., Grillo, M., Smith-Roe, S.L., Kang, T.H., Cordeiro-Stone, M., Kaufmann, W.K., Abraham, R.T., Sancar, A., and Unsal-Kaçmaz, K. (2010). Tipin-replication protein A interaction mediates Chk1 phosphorylation by ATR in response to genotoxic stress. J. Biol. Chem. *285*, 16562–16571.

Kibe, T., Zimmermann, M., and de Lange, T. (2016). TPP1 Blocks an ATR-Mediated Resection Mechanism at Telomeres. Mol. Cell *61*, 236–246.

Kobayashi, M., Hayashi, N., Takata, M., and Yamamoto, K. (2013). NBS1 directly activates ATR independently of MRE11 and TOPBP1. Genes Cells *18*, 238–246.

Kratz, K., and de Lange, T. (2018). Protection of telomeres 1 proteins POT1a and POT1b can repress ATR signaling by RPA exclusion, but binding to CST limits ATR repression by POT1b. J. Biol. Chem. *293*, 14384–14392.

Kumagai, A., Kim, S.M., and Dunphy, W.G. (2004). Claspin and the activated form of ATR-ATRIP collaborate in the activation of Chk1. J. Biol. Chem. *279*, 49599–49608.

Lam, Y.C., Akhter, S., Gu, P., Ye, J., Poulet, A., Giraud-Panis, M.J., Bailey, S.M., Gilson, E., Legerski, R.J., and Chang, S. (2010). SNMIB/Apollo protects leading-strand telomeres against NHEJ-mediated repair. EMBO J. *29*, 2230–2241.

Lee, J., and Dunphy, W.G. (2010). Rad17 plays a central role in establishment of the interaction between TopBP1 and the Rad9-Hus1-Rad1 complex at stalled replication forks. Mol. Biol. Cell *21*, 926–935.

Lee, J., Kumagai, A., and Dunphy, W.G. (2003). Claspin, a Chk1-regulatory protein, monitors DNA replication on chromatin independently of RPA, ATR, and Rad17. Mol. Cell *11*, 329–340.

Lee-Theilen, M., Matthews, A.J., Kelly, D., Zheng, S., and Chaudhuri, J. (2011). CtIP promotes microhomology-mediated alternative end joining during class-switch recombination. Nat. Struct. Mol. Biol. *18*, 75–79.

Leman, A.R., Dheekollu, J., Deng, Z., Lee, S.W., Das, M.M., Lieberman, P.M., and Noguchi, E. (2012). Timeless preserves telomere length by promoting efficient DNA replication through human telomeres. Cell Cycle *11*, 2337–2347.

Lengsfeld, B.M., Rattray, A.J., Bhaskara, V., Ghirlando, R., and Paull, T.T. (2007). Sae2 is an endonuclease that processes hairpin DNA cooperatively with the Mre11/Rad50/Xrs2 complex. Mol. Cell *28*, 638–651.

Lieber, M.R. (2010). The mechanism of double-strand DNA break repair by the nonhomologous DNA end-joining pathway. Annu. Rev. Biochem. *79*, 181–211.

Lin, Y.F., Shih, H.Y., Shang, Z., Matsunaga, S., and Chen, B.P. (2014). DNA-PKcs is required to maintain stability of Chk1 and Claspin for optimal replication stress response. Nucleic Acids Res. *42*, 4463–4473.

Lindsey-Boltz, L.A., Serçin, O., Choi, J.H., and Sancar, A. (2009). Reconstitution of human claspin-mediated phosphorylation of Chk1 by the ATR (ataxia telangiectasia-mutated and rad3-related) checkpoint kinase. J. Biol. Chem. *284*, 33107–33114.

MacDougall, C.A., Byun, T.S., Van, C., Yee, M.C., and Cimprich, K.A. (2007). The structural determinants of checkpoint activation. Genes Dev. *21*, 898–903.

Makharashvili, N., Tubbs, A.T., Yang, S.H., Wang, H., Barton, O., Zhou, Y., Deshpande, R.A., Lee, J.H., Lobrich, M., Sleckman, B.P., et al. (2014). Catalytic and noncatalytic roles of the CtIP endonuclease in double-strand break end resection. Mol. Cell *54*, 1022–1033.

Manthey, K.C., Opiyo, S., Glanzer, J.G., Dimitrova, D., Elliott, J., and Oakley, G.G. (2007). NBS1 mediates ATR-dependent RPA hyperphosphorylation following replication-fork stall and collapse. J. Cell Sci. *120*, 4221–4229.

Mateos-Gomez, P.A., Gong, F., Nair, N., Miller, K.M., Lazzerini-Denchi, E., and Sfeir, A. (2015). Mammalian polymerase θ promotes alternative NHEJ and suppresses recombination. Nature *518*, 254–257.

Mateos-Gomez, P.A., Kent, T., Deng, S.K., McDevitt, S., Kashkina, E., Hoang, T.M., Pomerantz, R.T., and Sfeir, A. (2017). The helicase domain of Polθ counteracts RPA to promote alt-NHEJ. Nat. Struct. Mol. Biol. *24*, 1116–1123.

Matsuura, S., Kobayashi, J., Tauchi, H., and Komatsu, K. (2004). Nijmegen breakage syndrome and DNA double strand break repair by NBS1 complex. Adv. Biophys. *38*, 65–80.

Pinzaru, A.M., Hom, R.A., Beal, A., Phillips, A.F., Ni, E., Cardozo, T., Nair, N., Choi, J., Wuttke, D.S., Sfeir, A., and Denchi, E.L. (2016). Telomere Replication Stress Induced by POT1 Inactivation Accelerates Tumorigenesis. Cell Rep. *15*, 2170–2184.

Poole, L.A., Zhao, R., Glick, G.G., Lovejoy, C.A., Eischen, C.M., and Cortez, D. (2015). SMARCAL1 maintains telomere integrity during DNA replication. Proc. Natl. Acad. Sci. USA *112*, 14864–14869.

Przetocka, S., Porro, A., Bolck, H.A., Walker, C., Lezaja, A., Trenner, A., von Aesch, C., Himmels, S.F., D'Andrea, A.D., Ceccaldi, R., et al. (2018). CtIP-Mediated Fork Protection Synergizes with BRCA1 to Suppress Genomic Instability upon DNA Replication Stress. Mol. Cell *72*, 568–582.e6.

Rai, R., Zheng, H., He, H., Luo, Y., Multani, A., Carpenter, P.B., and Chang, S. (2010). The function of classical and alternative non-homologous end-joining pathways in the fusion of dysfunctional telomeres. EMBO J. *29*, 2598–2610.

Rai, R., Li, J.M., Zheng, H., Lok, G.T., Deng, Y., Huen, M.S., Chen, J., Jin, J., and Chang, S. (2011). The E3 ubiquitin ligase Rnf8 stabilizes Tpp1 to promote telomere end protection. Nat. Struct. Mol. Biol. *18*, 1400–1407.

Rai, R., Chen, Y., Lei, M., and Chang, S. (2016). TRF2-RAP1 is required to protect telomeres from engaging in homologous recombination-mediated deletions and fusions. Nat. Commun. *7*, 10881.

Rai, R., Hu, C., Broton, C., Chen, Y., Lei, M., and Chang, S. (2017). NBS1 Phosphorylation Status Dictates Repair Choice of Dysfunctional Telomeres. Mol. Cell *65*, 801–817.e4.

Rass, E., Grabarz, A., Plo, I., Gautier, J., Bertrand, P., and Lopez, B.S. (2009). Role of Mre11 in chromosomal nonhomologous end joining in mammalian cells. Nat. Struct. Mol. Biol. *16*, 819–824.

Reynolds, J.J., Bicknell, L.S., Carroll, P., Higgs, M.R., Shaheen, R., Murray, J.E., Papadopoulos, D.K., Leitch, A., Murina, O., Tarnauskaitė, Ž., et al. (2017). Mutations in DONSON disrupt replication fork stability and cause microcephalic dwarfism. Nat. Genet. *49*, 537–549.

Rizzo, A., Salvati, E., Porru, M., D'Angelo, C., Stevens, M.F., D'Incalci, M., Leonetti, C., Gilson, E., Zupi, G., and Biroccio, A. (2009). Stabilization of quadruplex DNA perturbs telomere replication leading to the activation of an ATR-dependent ATM signaling pathway. Nucleic Acids Res. *37*, 5353–5364.

Rodríguez-Bravo, V., Guaita-Esteruelas, S., Florensa, R., Bachs, O., and Agell, N. (2006). Chk1- and claspin-dependent but ATR/ATM- and Rad17-independent DNA replication checkpoint response in HeLa cells. Cancer Res. *66*, 8672–8679.

Sakaue-Sawano, A., Kurokawa, H., Morimura, T., Hanyu, A., Hama, H., Osawa, H., Kashiwagi, S., Fukami, K., Miyata, T., Miyoshi, H., et al. (2008). Visualizing spatiotemporal dynamics of multicellular cell-cycle progression. Cell *132*, 487–498.

Sar, F., Lindsey-Boltz, L.A., Subramanian, D., Croteau, D.L., Hutsell, S.Q., Griffith, J.D., and Sancar, A. (2004). Human claspin is a ring-shaped DNA-binding protein with high affinity to branched DNA structures. J. Biol. Chem. *279*, 39289–39295.

Sfeir, A., and de Lange, T. (2012). Removal of shelterin reveals the telomere end-protection problem. Science *336*, 593–597.

Sfeir, A., and Symington, L.S. (2015). Microhomology-Mediated End Joining: A Back-up Survival Mechanism or Dedicated Pathway? Trends Biochem. Sci. *40*, 701–714.

Sfeir, A., Kosiyatrakul, S.T., Hockemeyer, D., MacRae, S.L., Karlseder, J., Schildkraut, C.L., and de Lange, T. (2009). Mammalian telomeres resemble fragile sites and require TRF1 for efficient replication. Cell *138*, 90–103.

Smits, V.A.J., Cabrera, E., Freire, R., and Gillespie, D.A. (2019). Claspin - checkpoint adaptor and DNA replication factor. FEBS J. *286*, 441–455.

Sotiriou, S.K., Kamileri, I., Lugli, N., Evangelou, K., Da-Ré, C., Huber, F., Padayachy, L., Tardy, S., Nicati, N.L., Barriot, S., et al. (2016). Mammalian RAD52 Functions in Break-Induced Replication Repair of Collapsed DNA Replication Forks. Mol. Cell *64*, 1127–1134.

Stiff, T., Reis, C., Alderton, G.K., Woodbine, L., O'Driscoll, M., and Jeggo, P.A. (2005). Nbs1 is required for ATR-dependent phosphorylation events. EMBO J. *24*, 199–208.

Symington, L.S. (2016). Mechanism and regulation of DNA end resection in eukaryotes. Crit. Rev. Biochem. Mol. Biol. *51*, 195–212.

Tenorio-Gómez, M., de Sena-Tomás, C., and Pérez-Martín, J. (2015). MRN- and 9-1-1-Independent Activation of the ATR-Chk1 Pathway during the Induction of the Virulence Program in the Phytopathogen Ustilago maydis. PLoS One *10*, e0137192.

Tomimatsu, N., Mukherjee, B., Catherine Hardebeck, M., Ilcheva, M., Vanessa Camacho, C., Louise Harris, J., Porteus, M., Llorente, B., Khanna, K.K., and Burma, S. (2014). Phosphorylation of EXO1 by CDKs 1 and 2 regulates DNA end resection and repair pathway choice. Nat. Commun. *5*, 3561.

Truong, L.N., Li, Y., Shi, L.Z., Hwang, P.Y., He, J., Wang, H., Razavian, N., Berns, M.W., and Wu, X. (2013). Microhomology-mediated end joining and homologous recombination share the initial end resection step to repair DNA

double-strand breaks in mammalian cells. Proc. Natl. Acad. Sci. USA *110*, 7720–7725.

Vannier, J.B., Pavicic-Kaltenbrunner, V., Petalcorin, M.I., Ding, H., and Boulton, S.J. (2012). RTEL1 dismantles T loops and counteracts telomeric G4-DNA to maintain telomere integrity. Cell *149*, 795–806.

Vannier, J.B., Sandhu, S., Petalcorin, M.I., Wu, X., Nabi, Z., Ding, H., and Boulton, S.J. (2013). RTEL1 is a replisome-associated helicase that promotes telomere and genome-wide replication. Science *342*, 239–242.

Verdun, R.E., and Karlseder, J. (2007). Replication and protection of telomeres. Nature *447*, 924–931.

Verma, P., and Greenberg, R.A. (2016). Noncanonical views of homology-directed DNA repair. Genes Dev. *30*, 1138–1154.

Wang, H., Rosidi, B., Perrault, R., Wang, M., Zhang, L., Windhofer, F., and Iliakis, G. (2005). DNA ligase III as a candidate component of backup pathways of nonhomologous end joining. Cancer Res. *65*, 4020–4030.

Wang, H., Li, Y., Truong, L.N., Shi, L.Z., Hwang, P.Y., He, J., Do, J., Cho, M.J., Li, H., Negrete, A., et al. (2014). CtIP maintains stability at common fragile sites and inverted repeats by end resection-independent endonuclease activity. Mol. Cell *54*, 1012–1021.

Wu, L., Multani, A.S., He, H., Cosme-Blanco, W., Deng, Y., Deng, J.M., Bachilo, O., Pathak, S., Tahara, H., Bailey, S.M., et al. (2006). Pot1 deficiency initiates DNA damage checkpoint activation and aberrant homologous recombination at telomeres. Cell *126*, 49–62.

Wu, P., van Overbeek, M., Rooney, S., and de Lange, T. (2010). Apollo contributes to G overhang maintenance and protects leading-end telomeres. Mol. Cell *39*, 606–617.

Wu, P., Takai, H., and de Lange, T. (2012). Telomeric 3′ overhangs derive from resection by Exo1 and Apollo and fill-in by POT1b-associated CST. Cell *150*, 39–52.

Xie, A., Kwok, A., and Scully, R. (2009). Role of mammalian Mre11 in classical and alternative nonhomologous end joining. Nat. Struct. Mol. Biol. *16*, 814–818.

Xin, H., Liu, D., Wan, M., Safari, A., Kim, H., Sun, W., O'Connor, M.S., and Songyang, Z. (2007). TPP1 is a homologue of ciliate TEBP-beta and interacts with POT1 to recruit telomerase. Nature *445*, 559–562.

Yang, Y.G., Saidi, A., Frappart, P.O., Min, W., Barrucand, C., Dumon-Jones, V., Michelon, J., Herceg, Z., and Wang, Z.Q. (2006). Conditional deletion of Nbs1 in murine cells reveals its role in branching repair pathways of DNA double-strand breaks. EMBO J. *25*, 5527–5538.

Yang, X.H., Shiotani, B., Classon, M., and Zou, L. (2008). Chk1 and Claspin potentiate PCNA ubiquitination. Genes Dev. *22*, 1147–1152.

Yang, C.C., Suzuki, M., Yamakawa, S., Uno, S., Ishii, A., Yamazaki, S., Fukatsu, R., Fujisawa, R., Sakimura, K., Tsurimoto, T., and Masai, H. (2016). Claspin recruits Cdc7 kinase for initiation of DNA replication in human cells. Nat. Commun. *7*, 12135.

Yu, T.Y., Kimble, M.T., and Symington, L.S. (2018). Sae2 antagonizes Rad9 accumulation at DNA double-strand breaks to attenuate checkpoint signaling and facilitate end resection. Proc. Natl. Acad. Sci. USA *115*, E11961–E11969.

Yuan, J., and Chen, J. (2010). MRE11-RAD50-NBS1 complex dictates DNA repair independent of H2AX. J. Biol. Chem. *285*, 1097–1104.

Yusufzai, T., and Kadonaga, J.T. (2008). HARP is an ATP-driven annealing helicase. Science *322*, 748–750.

Zaug, A.J., Podell, E.R., and Cech, T.R. (2005). Human POT1 disrupts telomeric G-quadruplexes allowing telomerase extension in vitro. Proc. Natl. Acad. Sci. USA *102*, 10864–10869.

Zhang, Y., and Jasin, M. (2011). An essential role for CtIP in chromosomal translocation formation through an alternative end-joining pathway. Nat. Struct. Mol. Biol. *18*, 80–84.

Zou, L., and Elledge, S.J. (2003). Sensing DNA damage through ATRIP recognition of RPA-ssDNA complexes. Science *300*, 1542–1548.

Zou, L., Cortez, D., and Elledge, S.J. (2002). Regulation of ATR substrate selection by Rad17-dependent loading of Rad9 complexes onto chromatin. Genes Dev. *16*, 198–208.

STAR★METHODS

KEY RESOURCES TABLE

REAGENT or RESOURCE	SOURCE	IDENTIFIER
Antibodies		
Rabbit anti phospho-CHK1	Cell Signaling Technology	2348; RRID: AB_331212
Mouse anti phospho-CHK2	BD Biosciences	611570; RRID: AB_399016
Mouse anti γ-H2AX	Millipore	05-636; RRID: AB_309864
Mouse anti-TRF2	Millipore	05-521; RRID: AB_2303145
Mouse anti-Myc	Millipore	05-724, RRID: AB_309938
Rabbit anti-RAD51	Santacruz	sc-8349, RRID: AB_2253533
Mouse anti-BRCA1	Santacruz	sc-6954, RRID: AB_626761
Rabbit anti-BARD1	Santacruz	sc-11438; RRID: AB_2061240
Rabbit anti-CTIP	Santacruz	sc-22838, RRID: AB_2175257
Mouse anti-SMARCAL1	Santacruz	sc-376377, RRID: AB_10987841
Rabbit anti-PCNA	Santacruz	sc-7907, RRID: AB_2160375
Mouse anti-GFP	Santacruz	sc-9996; RRID: AB_627695
Rabbit anti-53BP1	Santacruz	sc-22760; RRID: AB_2256326
Rabbit anti-EXO1	Santacruz	sc-33194, RRID: AB_2101433
Mouse RAD52	Santacruz	sc-365341, RRID: AB_10851346
Mouse anti-Flag	Sigma-Aldrich	F3165; RRID: AB_259529
Mouse anti-HA	Sigma-Aldrich	H3663; RRID: AB_262051
Rabbit anti-V5	Sigma-Aldrich	V8137, RRID: AB_261889
Mouse anti-γ-Tubulin (clone GTU-488)	Sigma-Aldrich	T6557; RRID: AB_477584
Mouse anti-Myc agarose beads	Sigma-Aldrich	A7470; RRID: AB_10109522
Mouse anti-Flag M2 affinity Gel	Sigma-Aldrich	A2220; RRID: AB_10063035
Mouse anti-HA agarose beads	Sigma-Aldrich	A2095, RRID: AB_257974
Rabbit anti-DONSON	Sigma-Aldrich	AV45862, RRID: AB_1847828
Rabbit anti-DONSON	Invitrogen	PA5-61865, RRID: AB_2640751
Rabbit anti-Claspin	Abcam	ab3720, RRID: AB_2245123
Rabbit anti-Claspin	Novus	NB100-248, RRID: AB_2082897
Rabbit anti-Claspin	Bethyl Laboratories	A300-266A, RRID: AB_155895
Rabbit anti phospho-RPA32 (S4/S8)	Bethyl Laboratories	A300-245A, RRID: AB_210547
Mouse anti PCNA	Bio-Rad	VMA00018
Rabbit anti-mTRF2	Karlsedar Lab	N/A
Streptavidin-Agarose resin	Thermo Scientific	20359
Bacterial and Virus Strains		
XL1-Blue Supercompetent cells	Agilent Technologies	200518
XL10-Gold Ultracompetent Cells	Agilent Technologies	200315
Chemicals, Peptides, and Recombinant Proteins		
DNA-PKcs inhibitor NU7441	Selleckchem	S2638
Critical Commercial Assays		
Site-directed mutagenesis	Stratagene	200521
TRAPeze Telomerase Detection Kit	Fisher Scientific	S7700
Experimental Models: Cell Lines		
Human *NBS-ILB1* cells	Falck et al., 2012, EMBO Reports.	N/A
U2OS	ATCC	N/A
293T	ATCC	CRL-3216, RRID: CVCL_0063

(*Continued on next page*)

Continued

REAGENT or RESOURCE	SOURCE	IDENTIFIER
Nbs1$^{-/-}$ MEFs	Matsuura et al., 2004, Adv Biophys.	N/A
Apollo/SNM1B$^{-/-}$ MEFs	Lam et al., 2010, EMBO J.	N/A
G1 mTR$^{-/-}$ MEFs	This paper	N/A
MMTV-Cre^{+}*; Pot1a*$^{F/\Delta}$*; p53*$^{\Delta/\Delta}$ MEFs	Gu et al., 2017	N/A
MMTV-Cre^{+}*; Pot1a* $^{\Delta/\Delta}$*; p53*$^{\Delta/\Delta}$ MEFs		
Experimental Models: Organisms/Strains		
MMTV-Cre^{+}*; Pot1a*$^{F/F}$*; p53*$^{F/F}$ mouse tumor model	Gu et al., 2017	N/A
Oligonucleotides		
Biotin-Tel-G $(TTAGGG)_6$	This paper	N/A
Biotin-Tel-C $(CCCTAA)_6$	This paper	N/A
Biotin Oligo $(dT)_6$	This paper	N/A
TelC-Cy3 $(CCCTAA)_3$	PNABio	F1002
TelG-FAM $(TTAGGG)_3$	PNABio	F1005
Recombinant DNA		
pBabe puro Myc-hTRF2$^{\Delta B\Delta M}$	Rai et al., 2017, Molecular Cell	N/A
pQCXIP puro Flag-hTPP1$^{\Delta RD}$	Rai et al., 2017, Molecular Cell	N/A
pQCXIP puro HA-hTPP1$^{\Delta RD}$	Rai et al., 2017, Molecular Cell	N/A
pQCXIP puro HA-mTPP1$^{\Delta RD}$	Rai et al., 2017, Molecular Cell	N/A
pQCXIP puro Flag-mTPP1$^{\Delta RD}$	Rai et al., 2017, Molecular Cell	NA
pQCXIP puro Flag-mNBS1^{WT}	Rai et al., 2017, Molecular Cell	N/A
pQCXIP Flag-TIN2^{A110R}	Hu et al., 2017, Cell Res.	N/A
pQCXIP Myc-mPOT1a and OB fold mutant mPOT1a^{F62A}	Wu et al., 2006, Cell	N/A
pCDNA3.1 Myc-TRF2	Chen et al., 2011, NSMB	N/A
pEGFP-EXO1	Tomimatsu et al., 2014, Nature Comm.	N/A
pLenti V5-EXO1	Tomimatsu et al., 2014, Nature Comm.	N/A
Fucci mKO-CTD1	Sakaue-Sawano et al., 2008, Cell	N/A
Fucci mAG-Geminin	Sakaue-Sawano et al., 2008, Cell	N/A
pGEX4T1 Human N-Terminal, C-Terminal, WT and Claspin 3A mutant	Lindsey-Boltz et al., 2009, JBC	N/A
pQCXIP HA-hClaspin WT and mutants	This paper	N/A
pQCXIP HA-mClaspin WT and mutants	This paper	N/A
pQCXIP HA-mPCNA	This paper	N/A
pCMV6 Myc-mPCNA	Origene	RC209379
pQCXIP Myc hDonson	This paper	N/A
pEGFP-DONSON and disease mutants	Reynolds et al., 2017	N/A
Flag-ATRIP	Lee Zou (Harvard Medical School)	N/A
pRetroSuper sh*Trf2*	Deng et al., 2009	N/A
pMKO.1 sh*BRCA1*	Xiaohua Wu (Scrips Research Institute)	N/A
pRetroSuper sh*Parp1*	Madalena Tarsounas (University of Oxford)	N/A
pRetroSuper sh*Ligase 3*	Madalena Tarsounas	N/A
pRetroSuper sh*Rad51*	Madalena Tarsounas	N/A
pGIPZ sh*Claspin*	Zhenkun Lou (Mayo Clinic)	N/A
pGIPZ sh*Rad52*	Ryan Jensen (Yale University)	V2LHS_171206
		V3LHS_376616
PIK.01 Lenti sh*Polq*	Agnel Sfeir (NYU)	N/A
PIK.01 Lenti sh*Ctip*	Sigma-Aldrich	TRCN0000305376

(*Continued on next page*)

Continued		
REAGENT or RESOURCE	SOURCE	IDENTIFIER
PIK.01 Lenti sh*Exo1*	Sigma-Aldrich	TRCN0000218614
		TRCN0000238466
		TRCN0000238468
PIK.01 Lenti sh*Claspin*	Sigma-Aldrich	TRCN0000193573
		TRCN0000175992
		TRCN0000193398
PIK.01 Lenti sh*Pcna*	Sigma-Aldrich	TRCN0000294872
		TRCN0000294805
		TRCN0000287377
PIK.01 Lenti sh*Donson*	Sigma-Aldrich	TRCN0000377075
		TRCN0000249773
		TRCN0000201175
PIK.01 Lenti sh*PCNA*	Sigma-Aldrich	TRCN0000003862
		TRCN0000003864
PIK.01 Lenti sh*DONSON*	Sigma-Aldrich	TRCN0000275364
		TRCN0000275365
		TRCN0000275367
Software and Algorithms		
GraphPad Prism Software (Version 7)	San Diego, CA	RRID:SCR_002798
NIS-Elements BR (Verson3.2)	Nikon	RRID:SCR_002776
Origin 7 software	OriginLab	N/A
ImageQuantTL	GE Healthcare	RRID:SCR_014246
FlowJo	FlowJo LLC	RRID:SCR_008520

LEAD CONTACT AND MATERIALS AVAILABILITY

Further information and requests for resources and reagents should be directed to and will be fulfilled by the Lead Contact, Dr. Sandy Chang (s.chang@yale.edu). All plasmids and cell lines generated in this study are available on request without restrictions.

EXPERIMENTAL MODEL AND SUBJECT DETAILS

Cell lines

Human *NBS-ILB1* cells, *Nbs1*$^{+/+}$, *Nbs1*$^{-/-}$, *G1 mTR*$^{-/-}$ and *Apollo/SNM1B*$^{-/-}$ MEFs and 293T were cultured in DMEM supplemented with 10% FBS and maintained in 5% CO2 at 37°C. U2OS cells were cultured in Macoy's medium. Source of U2OS, 293T and MEFs used in this study are listed in the Key Resources Table.

Mouse tumor model for generation of MMTV-Cre; mPot1a$^{F/F}$; p53$^{F/F}$ tumor cell lines

To generate *MMTV-Cre; mPot1a*$^{F/F}$*; p53*$^{F/F}$ mice, *MMTV-Cre* mice (The Jackson Laboratory, Tg (MMTV-cre) 4Mam/J; stock number: 003553) were first crossed with *mPot1a*$^{F/F}$ mice (Wu et al., 2006) to generate *MMTV-Cre; mPot1a*$^{F/F}$ mice. *MMTV-Cre; mPot1a*$^{F/F}$ mice were then crossed with *p53*$^{F/F}$ (The Jackson Laboratory, B6.129P2-Trp53tm1Brn/J; Stock No:008462) mice to generate *MMTV-Cre; mPot1a*$^{F/F}$*; p53*$^{F/+}$ and *MMTV-Cre; mPot1a*$^{F/F}$*; p53*$^{F/F}$ mice. *mPot1a*$^{F/F}$ and *mPot1a*$^{F/F}$*; p53*$^{F/F}$ mice were generated as controls. All mice were maintained under basic care conditions according to the IACUC-approved protocols of Yale University. Sick mice (age 7-12 months old; Table S1) were sacrificed and tumors were harvested from breast glands or other organs. Chopped tumors were digested with 0.25% trypsin at 37°C for 15min followed by collagenase D treatment at 37°C for 30 min. The digested suspension was filtered through 40μm cell strainer and isolated tumor cells were pelleted by centrifugation and expanded by passaging in the DMEM with 10% FBS culture media.

METHOD DETAILS

Retroviral infection

DNA constructs were transfected into 293T cells using Fugene 6 and packaged into retro or lentiviral particles. Viral supernatant was collected 48-72 h after transfection, filtered and directly used to infect immortalized MEFs or human cells.

Western blot analysis

For immunoblotting, trypsinized cells were lysed in urea lysis buffer (8 M urea, 50 mM Tris-HCl, pH 7.4, and 150 mM β-mercaptoethanol). The lysates were denatured and then resolved on SDS–PAGE gel. The separated proteins were then blotted on a nitrocellulose plus membrane (Amersham), blocked with blocking solution (5% non-fat dry milk in PBS/0.1% Tween-20) for at least 1 h and incubated with appropriate primary antibody in blocking solution at least 2 h at room temperature or overnight at 4 °C. The membranes were washed 3 × 5 min with PBS/0.1% Tween-20 and incubated with appropriate secondary antibody in blocking solution for 1 h at room temperature. Chemiluminescence detection was performed using an ECL Western Blotting Detection kit from GE Healthcare.

Immunofluorescence and fluorescent *in situ* hybridization

Cells grown on coverslips were fixed for 10 min in 2% (w/v) sucrose and 2% (v/v) paraformaldehyde at room temperature followed by PBS washes. Coverslips were blocked in 0.2% (w/v) fish gelatin and 0.5% (w/v) BSA in PBS. Cells were incubated with primary antibodies and after PBS washes, cells were incubated with appropriate Alexa fluor secondary antibodies followed by washes in PBS + 0.1% Triton. IF-FISH was carried out using a TelC-Cy3 PNA telomere probe (PNA Bio). DNA was stained with DAPI, and digital images captured using NIS-Elements BR (Nikon) with a Nikon Eclipse 80i microscope and an Andor CCD camera.

Coimmunoprecipitation

293T cells grown in 10 cm plates were co-transfected with epitope tag cDNAs or vector control. 48 h after transfection, cells were harvested and lysed in buffer (20 mM HEPES, pH 7.5, 10% glycerol, 1mM EDTA, 0.5% (v/v) NP-40). Supernatants were immunoprecipitated with appropriate endogenous or protein tagged antibody conjugated agarose beads (Sigma). Beads were washed thrice and eluted proteins analyzed by SDS-PAGE.

Isothermal titration calorimetry

The equilibrium dissociation constants between the WT and mutant $TRF2^{TRFH}$ and $Claspin^{TBM}$ peptides were determined using an iTC_{200} calorimeter (MicroCal). The enthalpies of binding between the $TRF2^{TRFH}$ domain and the $Claspin^{TBM}$ were measured at 20°C in 25 mM Tris-HCl (pH8.0) and 150 mM NaCl. ITC data were subsequently analyzed and fitted using Origin 7 software (OriginLab) with blank injections of peptides into buffer subtracted from the experimental titrations prior to data analysis.

DNA binding assay

To examine whether CPD complex bind to ss telomeric DNA *in vitro*, 293T cells expressing GFP DONSON or HA-Claspin lysed in TEB_{150} buffer (50 mM HEPES pH 7.3, 150 mM NaCl, 2 mM $MgCl_2$, 5 mM EGTA, 0.5% Triton X-100, 10% Glycerol, proteinase inhibitors) were incubated with streptavidin–agarose beads (Thermo-Fisher) coated with biotin-Tel-G $(TTAGGG)_6$ or TEL-C $(CCCTAA)_6$ or Oligo $(dT)_6$ DNA oligos overnight at 4 °C. $POT1a^{WT}$ and $POT1a^{F62}$ protein lysates used as positive control (Wu et al., 2006). Bound complexes were washed three times with the same buffer and eluted proteins analyzed by SDS-PAGE.

Cell Cycle analysis

For FACS analysis, cells washed in PBS fixed with 70% ice-cold ethanol by drop-wise mixing, and incubated for at least 24 h in −20°C. Cells washed twice with PBS and then resuspended in 0.5 mL PBS containing 50 μg/ml of propidium iodide and 100 μg/ml of RNase A. The samples were analyzed on a BD LSR Fortessa cytometer. Data analysis was performed using FlowJo software. Cell cycle dependent expression of Claspin in U2OS cells was determined using Fucci system based on fluorescent proteins with fragments of CDT1 and Geminin, for the G1 and S/G2 reporters, respectively (Sakaue-Sawano et al., 2008).

Chromosome analysis by telomere PNA-FISH and CO-FISH

Cells were treated with 0.5 μg/ml of Colcemid before harvest. Chromosomes were fixed and telomere PNA-FISH performed with a TelC-Cy3 probe (PNA Bio) as described (Rai et al., 2016; Wu et al., 2006). For CO-FISH, metaphase spreads were incubated sequentially with TelG-FAM and TelC-Cy3 probes. Images were captured as described above. The percent of chromosome fusions observed is defined as: total number of chromosome fusions in 30–50 metaphase spreads analyzed divided by the total number of chromosomes examined X 100%.

Telomere length analysis and G-Strand overhang assays

For in-gel detection of telomere length and G-stand overhang, a total of 1–2 × 10^6 cells were suspended in PBS, mixed 1:1 with 1.8% agarose in 1 × PBS and cast into plugs. The plugs were then digested overnight at 50 °C with 20 mg ml^{-1} Proteinase K (Roche) in 10 mM sodium phosphate (pH 7.2) and 0.5 mM EDTA and 1% sodium lauryl sarcosine. DNA in plugs were subsequently digested by *Hinf*1/*Rsa*1 overnight at 37 °C. The next morning, plugs were washed once with 1 × TE and equilibrated with 0.5 × TBE. The plugs were loaded onto a 0.8% agarose gel in 0.5 × TBE and run on a CHEF-DRII pulse field electrophoresis apparatus (Bio-Rad). The electrophoresis parameters were as follows: Initial pulse: 0.3 s, final pulse: 16 s, voltage: 6 V cm^{-1}, run time: 14 h. Dried gel pre-hybridized with Church mix for 2 h at 55 °C and hybridized overnight at 55 °C in Church mix with ^{32}P-labeled T_2AG_3 oligonucleotides. After hybridization, the gel was washed three times for 30 min with 4 × SSC/0.1% SDS at 37 °C, thrice with 4 × SSC/0.1% SDS at

55°C and exposed to a phosphoimager screen overnight. After exposure, the screen was scanned on a Typhoon Trio imager system and the gel was subsequently denatured and hybridized using the same probe.

QUANTIFICATION AND STATISTICAL ANALYSIS

Statistics for TIFs and chromosome fusions were determined in term of p value from one-way Anova using GraphPad Prism software (Version 7.0).

DATA AND CODE AVAILABILITY

This study did not generate/analyze datasets/code.

Cell Reports, Volume *29*

Supplemental Information

The Replisome Mediates A-NHEJ Repair of Telomeres Lacking POT1-TPP1 Independently of MRN Function

Rekha Rai, Peili Gu, Cayla Broton, Chandan Kumar-Sinha, Yong Chen, and Sandy Chang

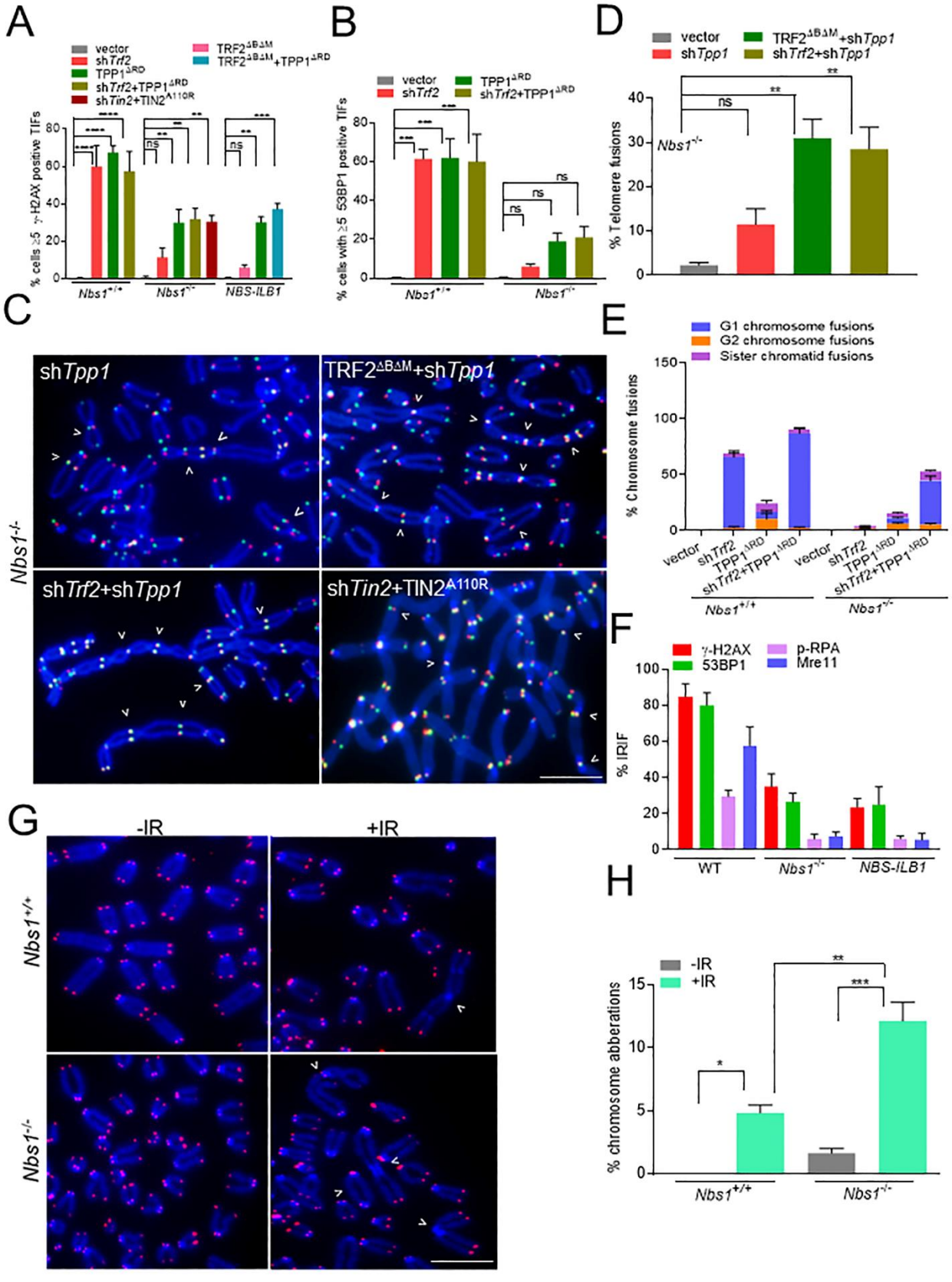
A
vector
shTrf2
TPP1ΔRD
shTrf2+TPP1ΔRD
shTin2+TIN2A110R
TRF2ΔBΔM
TRF2ΔBΔM+TPP1ΔRD
% cells ≥5 γ-H2AX positive TIFs
Nbs1+/+
Nbs1-/-
NBS-iLB1
B
vector
shTrf2
TPP1ΔRD
shTrf2+TPP1ΔRD
% cells with ≥5 53BP1 positive TIFs
Nbs1+/+
Nbs1-/-
D
vector
shTpp1
TRF2ΔBΔM+shTpp1
shTrf2+shTpp1
% Telomere fusions
Nbs1-/-
ns
C
shTpp1
TRF2ΔBΔM+shTpp1
shTrf2+shTpp1
shTin2+TIN2A110R
Nbs1-/-
E
G1 chromosome fusions
G2 chromosome fusions
Sister chromatid fusions
% Chromosome fusions
vector
shTrf2
TPP1ΔRD
shTrf2+TPP1ΔRD
Nbs1+/+
Nbs1-/-
F
γ-H2AX
53BP1
p-RPA
Mre11
% IRIF
WT
Nbs1-/-
NBS-iLB1
G
-IR
+IR
Nbs1+/+
Nbs1-/-
H
-IR
+IR
% chromosome abberations
Nbs1+/+
Nbs1-/-

Figure S1: Related to Figure 1

A. Quantification of percentage of *Nbs1*$^{+/+}$, *Nbs1*$^{-/-}$ or *NBS-ILB1* cells containing ≥5 γ-H2AX TIFs treated with the indicated DNAs. Data represents the mean of three independent experiments ± SD; n>250 nuclei analyzed per experiment. ***P*=0.005, ****P*=0.0007, *****P*<0.0001 by one-way ANOVA. ns: non-significant. **B**. Quantification of percentage of *Nbs1*$^{+/+}$ and *Nbs1*$^{-/-}$ MEFs containing ≥5 53BP1 TIFs treated with the indicated DNA constructs. Data represents the mean of three independent experiments ± SD; n>250 nuclei analyzed per experiment. ****P*=0.0003 by one-way ANOVA. ns: non-significant. **C**. *Nbs1*$^{-/-}$ MEFs were treated with the indicated DNA constructs for 120 h. TelG-FAM, TelC-Cy3 and DAPI (blue) were used to visualize fused chromosomes (arrowheads). **D**. Quantification of telomere fusion frequencies in (**C**). Data represents the average of two independent experiments ± SD from a minimum of 60 metaphases. ***P*=0.005 by one-way ANOVA. ns: non-significant. **E**. Quantification of chromosome fusions observed in *Nbs1*$^{+/+}$ and *Nbs1*$^{-/-}$ MEFs. Data represents the average of two independent experiments ± SD from a minimum of 80 metaphases. **F**. Quantification of percentage of cells containing ≥5 γ-H2AX, 53BP1, p-RPA32, and MRE11 foci in *Nbs1*$^{+/+}$, *Nbs1*$^{-/-}$ and *NBS-ILB1* cells treated with 2 Gy IR. **G**. *Nbs1*$^{+/+}$ and *Nbs1*$^{-/-}$ MEFs subjected to 2Gy IR. After 24h of irradiation, telomeres were visualized by PNA-FISH (red) and DAPI (blue). **H**. Quantification of chromosome aberrations detected in (**G**). Data represents the mean of two independent experiments ± SD from a minimum of 50 metaphases. **P*=0.01, ***P*=0.003, ****P*=0.0008 by one-way ANOVA. ns: non-significant.

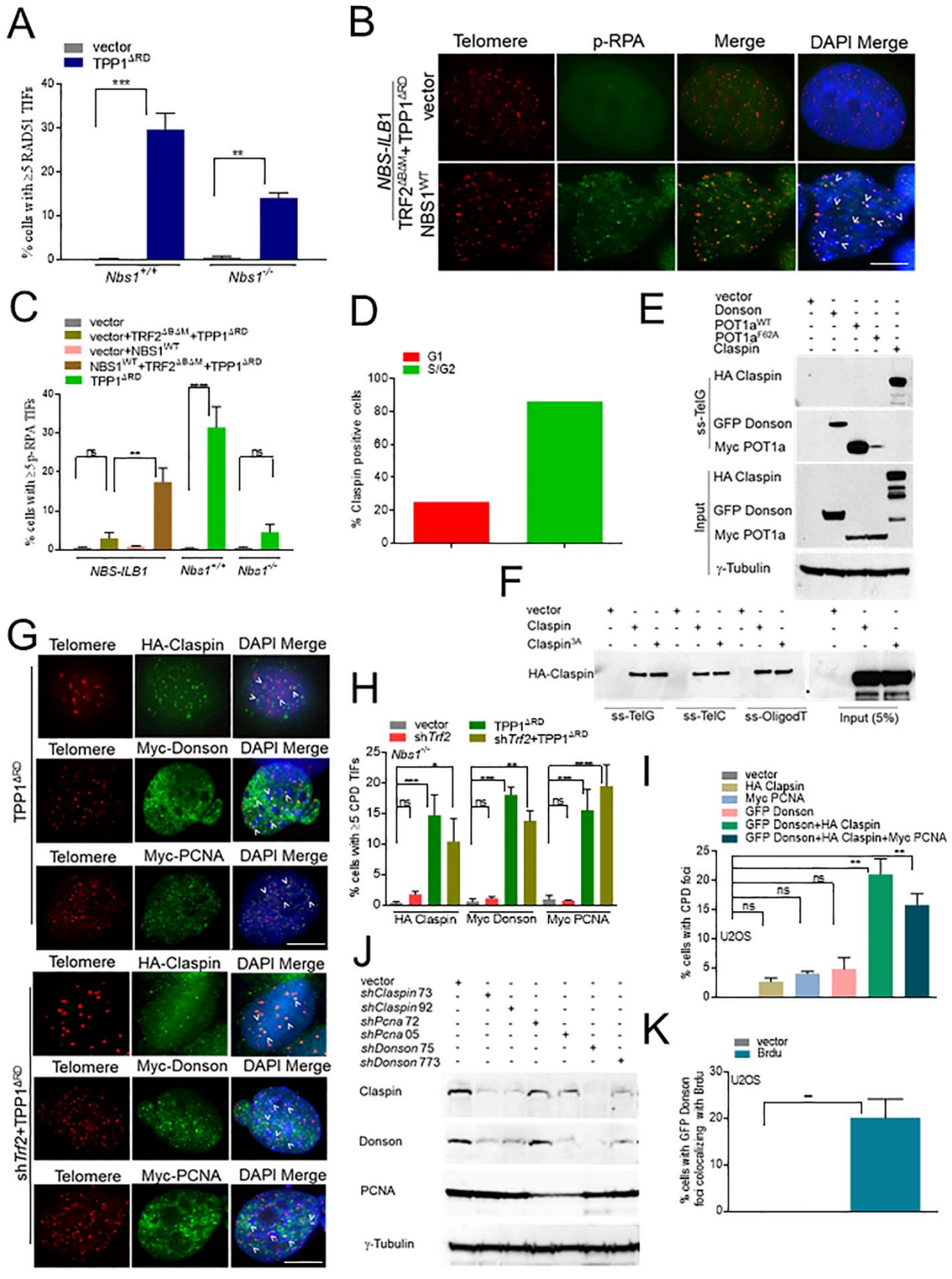
A
vector
TPP1ΔRD
% cells with ≥5 RAD51 TIFs
Nbs1+/+
Nbs1-/-
B
Telomere
p-RPA
Merge
DAPI Merge
NBS-ILB1
TRF2ΔB&M+TPP1ΔRD
vector
NBS1WT
C
vector
vector+TRF2ΔB&M+TPP1ΔRD
vector+NBS1WT
NBS1WT+TRF2ΔB&M+TPP1ΔRD
TPP1ΔRD
% cells with ≥5 γp-RPA TIFs
NBS-ILB1
Nbs1+/+
Nbs1-/-
D
G1
S/G2
% Claspin positive cells
E
vector
Donson
POT1aWT
POT1aF62A
Claspin
HA Claspin
GFP Donson
Myc POT1a
γ-Tubulin
ss-TelG
Input
F
vector
Claspin
Claspin3A
HA-Claspin
ss-TelG
ss-TelC
ss-OligodT
Input (5%)
G
Telomere
HA-Claspin
DAPI Merge
Myc-Donson
Myc-PCNA
TPP1ΔRD
shTrf2+TPP1ΔRD
H
vector
shTrf2
TPP1ΔRD
shTrf2+TPP1ΔRD
Nbs1-/-
% cells with ≥5 CPD TIFs
HA Claspin
Myc Donson
Myc PCNA
I
vector
HA Clapsin
Myc PCNA
GFP Donson
GFP Donson+HA Claspin
GFP Donson+HA Claspin+Myc PCNA
% cells with CPD foci
U2OS
J
vector
shClaspin73
shClaspin92
shPcna72
shPcna05
shDonson75
shDonson773
Claspin
Donson
PCNA
γ-Tubulin
K
vector
Brdu
U2OS
% cells with GFP Donson foci colocalizing with Brdu

Figure S2: Related to Figure 2

A. Quantification of percent of cells containing RAD51 positive TIFs in *Nbs1*$^{+/+}$ and *Nbs1*$^{-/-}$ MEFs. Data represents the mean of two independent experiments ± SD; n>150 nuclei analyzed per experiment. ***P*=0.007, ****P*=0.0004, by one-way ANOVA. **B**. p-RPA32 TIFs in *NBS-ILB1* cells expressing TRF2$^{\Delta B \Delta M}$ and TPP1$^{\Delta RD}$ were reconstituted with vector or with WT NBS1. Anti-p-RPA32 S4/S8 antibody was used to visualize p-RPA32 (green) and DAPI staining to visualize nuclei (blue). **C**. Quantification of percent of cells containing ≥5 p-RPA32 positive TIFs. Data represents the mean of two independent experiments ± SD; n>100 nuclei analyzed per experiment. ***P*=0.003, *****P*<0.0001 by one-way ANOVA. ns: non-significant. **D**. Quantification of percentage of U2OS cells with ≥ 5 HA-Claspin positive foci expressing mKO1-hCTD1(red, G1 phase) or mAG1-hGeminin (green, S/G2 phase). Data are the mean from two independent experiments ± SD; n>150 nuclei scored per experiment. **E**. 293T cells expressing the indicated epitope-tagged proteins were incubated with biotinylated single-stranded (ss) Tel-G $(TTAGGG)_6$ DNA, and DNA-protein complexes were isolated with streptavidin A. Bound proteins were eluted from the ss Tel-G, immunoblotted and detected with anti-GFP, anti-HA and anti-Myc antibodies. Inputs represent 5% of the total cell lysate used to perform protein-ss DNA binding experiments. γ-tubulin: loading control. **F**. 293T cells expressing the indicated epitope-tagged proteins were incubated with biotinylated single-stranded (ss) Tel-G $(TTAGGG)_6$, TEL-C $(CCCTAA)_6$ and Oligo $(dT)_6$ DNA, and DNA-protein complexes were isolated with streptavidin A. Bound proteins were eluted from DNA, immunoblotted and detected with anti-HA antibody. Inputs represent 5% of the total cell lysate used to perform protein- DNA binding experiments. **G**. *Nbs1*$^{-/-}$ MEFs expressing HA-Claspin, Myc-PCNA or Myc-DONSON were transfected with either TPP1$^{\Delta RD}$ or with sh*Trf2*-TPP1$^{\Delta RD}$. Telomeres were visualized by PNA-FISH (red), anti-HA antibody to visualize Claspin, and an anti-Myc antibody to visualize Myc-DONSON or Myc-PCNA. The arrowheads point to replisome proteins co-localizing with telomeres. **H**. Quantification of the percentage of cells containing ≥ 5 HA-Claspin, Myc-PCNA or Myc-DONSON (CPD) positive foci co-localizing with telomeres, detected in (**G**). Data represents the mean of three independent experiments ± SD; n>150 nuclei analyzed per experiment. **P*=0.01, ***P*=0.001, ****P*=0.0008, *****P*<0.0001 by one-way ANOVA. ns: non-significant. **I**. Quantification of percent of cells containing ≥ 5 HA-Claspin, Myc-PCNA or GFP-DONSON TIFs in U2OS cells. Data represents the mean of two independent experiments ± SD; n>200 nuclei analyzed per experiment. ***P*=0.001 by one-way ANOVA. ns: non-significant. **J**. Immunoblot to detect Claspin, PCNA and DONSON knockdown using the indicated shRNA in *Nbs1*$^{+/+}$ cells. γ-tubulin: loading control. **K**. Quantification of percent of cells containing ≥ 5 GFP-DONSON positive TIFs co-localizing with BrdU in U2OS cells. Cells were labelled with BrdU for 4h. Data represents the mean of two independent experiments ± SD; n>100 nuclei analyzed per experiment. ***P*=0.008 by one-way ANOVA. Scale bars 5μm.

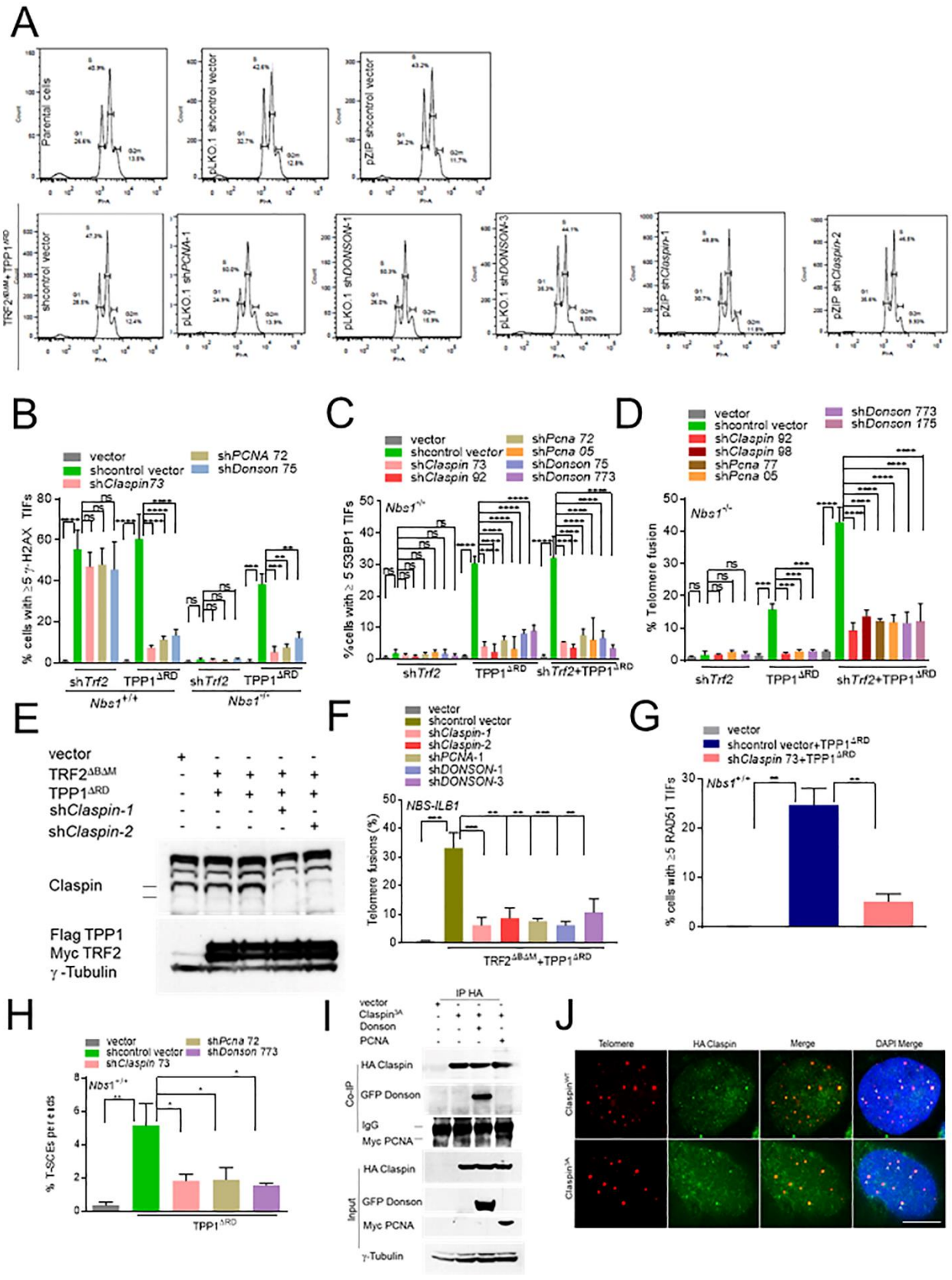
A
Parental cells
pLKO.1 shcontrol vector
pZIP shcontrol vector
TRF2ΔBΔM+TPP1ΔRD
shcontrol vector
pLKO.1 shPCNA-1
pLKO.1 shDONSON-1
pLKO.1 shDONSON-3
pZIP shClaspin-1
pZIP shClaspin-2
B
vector
shcontrol vector
shClaspin73
shPCNA 72
shDonson 75
% cells with ≥5 γ-H2AX TIFs
shTrf2
TPP1ΔRD
Nbs1+/+
Nbs1-/-
C
vector
shcontrol vector
shClaspin 73
shClaspin 92
shPcna 72
shPcna 05
shDonson 75
shDonson 773
%cells with ≥ 5 53BP1 TIFs
Nbs1-/-
shTrf2+TPP1ΔRD
D
vector
shcontrol vector
shClaspin 92
shClaspin 98
shPcna 77
shPcna 05
shDonson 773
shDonson 175
% Telomere fusion
E
vector
TRF2ΔBΔM
TPP1ΔRD
shClaspin-1
shClaspin-2
Claspin
Flag TPP1
Myc TRF2
γ -Tubulin
F
vector
shcontrol vector
shClaspin-1
shClaspin-2
shPCNA-1
shDONSON-1
shDONSON-3
NBS-ILB1
Telomere fusions (%)
TRF2ΔBΔM+TPP1ΔRD
G
vector
shcontrol vector+TPP1ΔRD
shClaspin 73+TPP1ΔRD
Nbs1+/+
% cells with ≥5 RAD51 TIFs
H
vector
shcontrol vector
shClaspin 73
shPcna 72
shDonson 773
Nbs1+/+
% T-SCEs per ends
TPP1ΔRD
I
IP HA
vector
ClaspinΔA
Donson
PCNA
HA Claspin
GFP Donson
IgG
Myc PCNA
Co-IP
Input
γ-Tubulin
J
Telomere
HA Claspin
Merge
DAPI Merge
ClaspinWT
ClaspinΔA

Figure S3: Related to Figure 3

A. Cell cycle analysis in *NBS-ILB1* cells depleted with CPD complex and indicated treatment. **B**. Quantification of percentage of *Nbs1*$^{+/+}$ *and Nbs1*$^{-/-}$ MEFs showing ≥ 5 γ-H2AX TIFs and expressing the indicated DNAs constructs. Data represents the mean of three independent experiments ± SD; n>300 nuclei analyzed per experiment. ***P*=0.001, ****P*=0.0001, *****P*<0.0001 by one-way ANOVA. ns: non-significant. **C**. Quantification of percentage of *Nbs1*$^{-/-}$ MEFs showing ≥ 5 53BP1 positive TIFs and expressing indicated DNAs constructs. Data represents the mean of three independent experiments ± SD; n>200 nuclei analyzed per experiment. *****P*<0.0001 by one-way ANOVA. ns: non-significant. **D**. Quantification of telomere fusion frequencies in *Nbs1*$^{-/-}$ cells treated with sh*Trf2* and TPP1$^{\Delta RD}$ or both. Data represents the average of two independent experiments ± SD from a minimum of 80 metaphases. ****P*=0.0001, *****P*<0.0001 by one-way ANOVA. ns: non-significant. **E**. Immunoblot showing Claspin knockdown using two shRNAs targeting *Claspin* in *NBS-ILB1* cells expressing indicated proteins. γ-tubulin: loading control. **F**. Quantification of telomere fusion frequencies in *NBS-ILB1* cells treated with TRF2$^{\Delta B\Delta M}$ *and* TPP1$^{\Delta RD}$ and shRNAs targeting *CPD*. Data represents the average of two independent experiments ± SD from a minimum of 80 metaphases. ***P*=0.001, ****P*=0.0001, by one-way ANOVA. **G**. Quantification of percent of cells with ≥ 5 RAD51 positive TIFs in cells expressing indicated DNAs. Data represents the mean of two independent experiments ± SD; n>150 nuclei analyzed per experiment**.** ***P*=0.001 by one-way ANOVA**. H**. Quantification of T-SCEs in cells with indicated DNAs. Data represents the average of two independent experiments ± SD from a minimum of 45 metaphases. **P*=0.01, ***P*=0.001 by one-way ANOVA. **I**. Co-IP of the indicated proteins transfected in 293T cells using anti-HA antibody. The inputs represent 5% of the total cell lysate used for the IP. γ -tubulin: loading control. **J**. Co-localization of WT HA-Claspin or the HA-Claspin^{3A} mutant in *Nbs1*$^{-/-}$ cells with telomeres. Telomeres were visualized by PNA-FISH (red), antibody staining (green), and DAPI (blue).

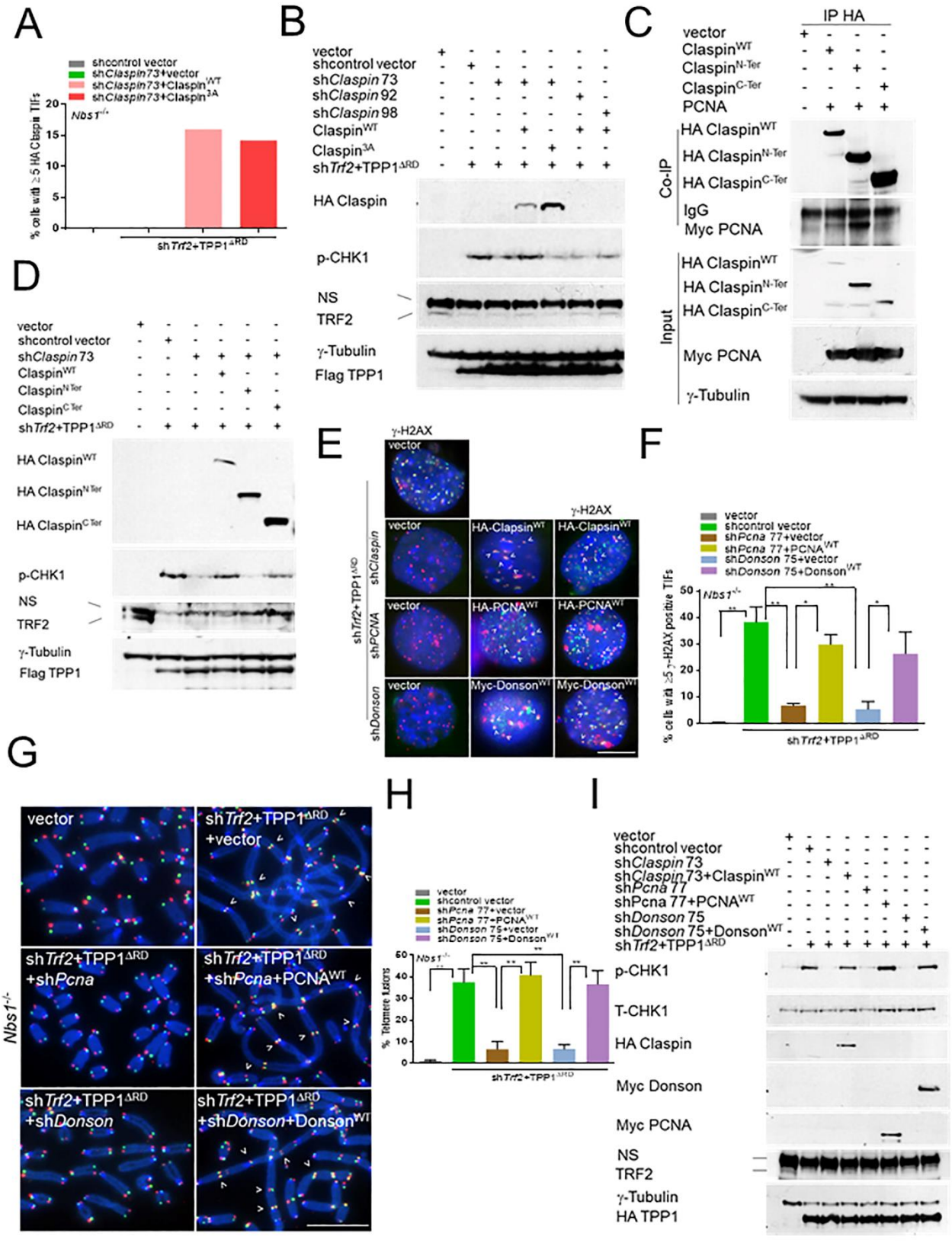
A
shcontrol vector
shClaspin73+vector
shClaspin73+ClaspinWT
shClaspin73+Claspin3A
Nbs1-/-
% cells with ≥5 HA Claspin TIFs
shTrf2+TPP1ΔRD
B
vector
shcontrol vector
shClaspin73
shClaspin92
shClaspin98
ClaspinWT
Claspin3A
shTrf2+TPP1ΔRD
HA Claspin
p-CHK1
NS
TRF2
γ-Tubulin
Flag TPP1
C
IP HA
vector
ClaspinWT
ClaspinN-Ter
ClaspinC-Ter
PCNA
Co-IP
HA ClaspinWT
HA ClaspinN-Ter
HA ClaspinC-Ter
IgG
Myc PCNA
Input
HA ClaspinWT
HA ClaspinN-Ter
HA ClaspinC-Ter
Myc PCNA
γ-Tubulin
D
vector
shcontrol vector
shClaspin73
ClaspinWT
ClaspinN Ter
ClaspinC Ter
shTrf2+TPP1ΔRD
HA ClaspinWT
HA ClaspinN Ter
HA ClaspinC Ter
p-CHK1
NS
TRF2
γ-Tubulin
Flag TPP1
E
γ-H2AX
vector
shTrf2+TPP1ΔRD
shClaspin
shPCNA
shDonson
HA-ClapsinWT
HA-PCNAWT
Myc-DonsonWT
F
vector
shcontrol vector
shPcna 77+vector
shPcna 77+PCNAWT
shDonson 75+vector
shDonson 75+DonsonWT
Nbs1-/-
% cells with ≥5 γ-H2AX positive TIFs
shTrf2+TPP1ΔRD
G
Nbs1-/-
vector
shTrf2+TPP1ΔRD +vector
shTrf2+TPP1ΔRD +shPcna
shTrf2+TPP1ΔRD +shPcna+PCNAWT
shTrf2+TPP1ΔRD +shDonson
shTrf2+TPP1ΔRD +shDonson+DonsonWT
H
vector
shcontrol vector
shPcna 77+vector
shPcna 77+PCNAWT
shDonson 75+vector
shDonson 75+DonsonWT
Nbs1-/-
% Telomere Lesions
shTrf2+TPP1ΔRD
I
vector
shcontrol vector
shClaspin73
shClaspin73+ClaspinWT
shPcna 77
shPcna 77+PCNAWT
shDonson 75
shDonson 75+DonsonWT
shTrf2+TPP1ΔRD
p-CHK1
T-CHK1
HA Claspin
Myc Donson
Myc PCNA
NS
TRF2
γ-Tubulin
HA TPP1

Figure S4: Related to Figure 3

A. Quantification of percentage of cells containing ≥ 5 WT HA-Claspin or HA-Claspin^{3A} at telomeres in *Nbs1*$^{-/-}$ MEFs expressing indicated DNAs constructs. **B**. Immunoblot for p-CHK1 levels in *Nbs1*$^{-/-}$ cells expressing shRNA resistant WT HA-Claspin or the HA-Claspin^{3A} mutant. γ-tubulin: loading control. shRNAs Claspin 92 and 98 target the Claspin coding sequences whereas shRNA Claspin 73 targets the UTR. Reconstituted WT Claspin or the 3A mutant cDNAs are resistant only to shRNA Claspin 73. **C**. Co-IP of the indicated proteins transfected in 293T cells using the anti-HA antibody. The inputs represent 5% of the total cell lysate used for the IP. γ -tubulin: loading control. **D**. Immunoblot for p-CHK1 levels in *Nbs1*$^{-/-}$ cells expressing WT HA-Claspin, HA-Claspin$^{N\text{-}ter}$ or HA-Claspin$^{C\text{-}ter}$. γ-tubulin: loading control. **E.** Immuno-FISH showing CPD and γ-H2AX co-localization with telomeres (arrowheads) in *Nbs1*$^{-/-}$ MEFs complemented with shRNA resistant CPD complex. Scale bars 5μm. **F.** Quantification of percentage of *Nbs1*$^{-/-}$ MEFs showing ≥ 5 γ-H2AX TIFs and expressing the indicated DNAs constructs. Data represents the mean of two independent experiments ± SD; n>200 nuclei analyzed per experiment. **P*=0.01, ***P*=0.001, by one-way ANOVA. **G.** Chromosome fusions in *Nbs1*$^{-/-}$ cells expressing shRNA resistant CPD complex and indicated DNA constructs for 120 h. TelG-FAM, TelC-Cy3 and DAPI (blue) were used to visualize fused chromosomes (arrowheads). **H.** Quantification of telomere fusion frequencies in (**G**). Data represents the average of two independent experiments ± SD from a minimum of 50 metaphases. ***P*=0.001 by one-way ANOVA. **I.** Immunoblot for p-CHK1 levels in *Nbs1*$^{-/-}$ cells expressing WT CPD complex and indicated constructs. γ-tubulin: loading control.

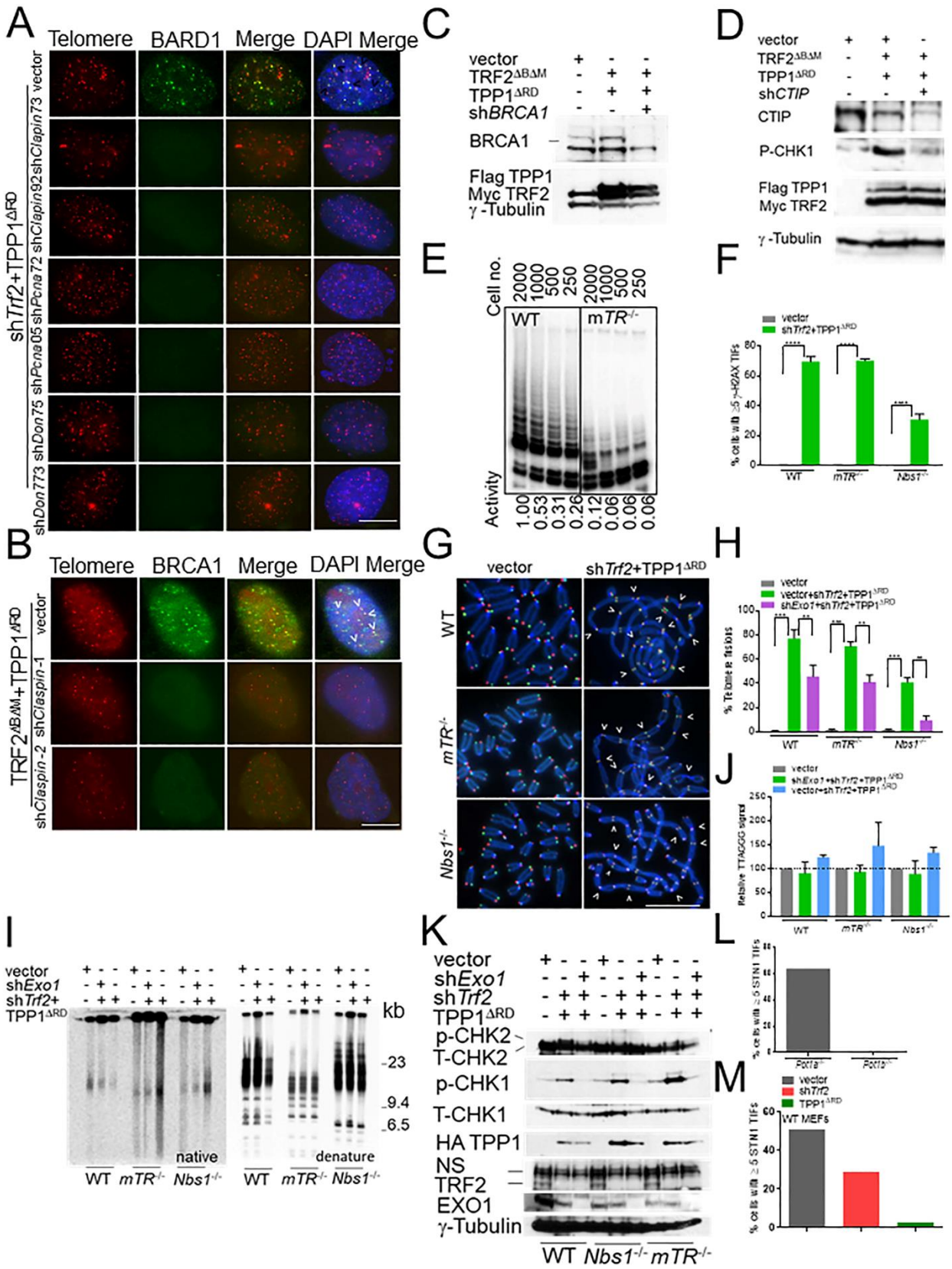
A
Telomere
BARD1
Merge
DAPI Merge
shTrf2+TPP1ΔRD
vector
shClapin73
shClapin92
shPcna72
shPcna05
shDon75
shDon773
B
Telomere
BRCA1
Merge
DAPI Merge
TRF2ΔBΔM+TPP1ΔRD
vector
shClaspin-1
shClaspin-2
C
vector
TRF2ΔBΔM
TPP1ΔRD
shBRCA1
BRCA1
Flag TPP1
Myc TRF2
γ-Tubulin
D
vector
TRF2ΔBΔM
TPP1ΔRD
shCTIP
CTIP
P-CHK1
Flag TPP1
Myc TRF2
γ-Tubulin
E
Cell no.
2000
1000
500
250
WT
mTR-/-
Activity
1.00
0.53
0.31
0.26
0.12
0.06
0.06
0.06
F
vector
shTrf2+TPP1ΔRD
% cells with ≥5 γ-H2AX TIFs
WT
mTR-/-
Nbs1-/-
G
vector
shTrf2+TPP1ΔRD
WT
mTR-/-
Nbs1-/-
H
vector
vector+shTrf2+TPP1ΔRD
shExo1+shTrf2+TPP1ΔRD
% Telomere fusions
WT
mTR-/-
Nbs1-/-
J
vector
shExo1+shTrf2+TPP1ΔRD
vector+shTrf2+TPP1ΔRD
Relative TTAGGG signal
WT
mTR-/-
Nbs1-/-
I
vector
shExo1
shTrf2+
TPP1ΔRD
kb
23
9.4
6.5
native
denature
WT
mTR-/-
Nbs1-/-
K
vector
shExo1
shTrf2
TPP1ΔRD
p-CHK2
T-CHK2
p-CHK1
T-CHK1
HA TPP1
NS
TRF2
EXO1
γ-Tubulin
WT
Nbs1-/-
mTR-/-
L
% cells with ≥5 53BP1 TIFs
Parp1+/+
Parp1-/-
M
vector
shTrf2
TPP1ΔRD
WT MEFs
% cells with ≥5 53BP1 TIFs

Figure S5: Related to Figure 5

Telomeric localization of BARD1 (**A**) and BRCA1 (**B**) in *Nbs1*$^{-/-}$ MEFs and *NBS-ILB1* treated with indicated shRNAs. Telomeres were visualized with PNA-FISH (red), antibodies were used to visualize the presence of BARD1 or BRCA1 on telomeres (green), and DAPI to visualize nuclei (blue). **C**. Immunoblot showing the knockdown of BRCA1 in *NBS-ILB1* cells expressing the indicated DNA constructs. γ-tubulin: loading control. **D**. Immunoblot showing the knockdown of CTIP in *NBS-ILB1* cells expressing indicated DNA constructs. γ-tubulin: loading control. **E.** Telomerase activity determined by TRAP assay in cells of indicated genotype. Telomerase activity was measured relative to the control and normalized to the internal control**. F.** Quantification of percentage of *Nbs1*$^{+/+}$, *Nbs1*$^{-/-}$ *and mTR*$^{-/-}$ MEFs showing ≥ 5 γ-H2AX TIFs and expressing the indicated DNAs constructs. Data represents the mean of two independent experiments ± SD; n>150 nuclei analyzed per experiment. ****P<0.0001, by one-way ANOVA.**G.** Chromosome fusions in *Nbs1*$^{+/+}$, *mTR*$^{-/-}$ *and Nbs1*$^{-/-}$ cells expressing indicated DNA constructs for 120 h. TelG-FAM, TelC-Cy3 and DAPI (blue) were used to visualize fused chromosomes (arrowheads). **H.** Quantification of telomere fusion frequencies in (**G**). Data represents the average of two independent experiments ± SD from a minimum of 70 metaphases. **P=0.001, ***P=0.0001, by one-way ANOVA. **I**. ss-DNA overhang in *Nbs1*$^{+/+}$, *mTR*$^{-/-}$ *and Nbs1*$^{-/-}$ cells expressing indicated DNA constructs and shRNA targeting EXO1 using in-gel hybridization with radiolabeled $(CCCTAA)_4$ probes to detect 3′ single-stranded overhang under native conditions (left) and under denaturing conditions to detect total TTAGGG repeats (right). Molecular weights are displayed on the right. **J**. Quantification of telomeric overhang signals determined in (**I**). Single stranded TTAGGG signals were normalized to the total TTAGGG signal in the same lane. The normalized signal for cells treated with vector control shRNA was set to 100, and all other values are displayed relative to this value. **K**. Reduced CHK1 phosphorylation in *Nbs1*$^{+/+}$, *mTR*$^{-/-}$ *and Nbs1*$^{-/-}$ MEFs expressing sh*Trf2* and TPP1$^{\Delta RD}$ treated with shRNA targeting EXO1. Immunoblots were examined for the level of total (T)-CHK1, T-CHK2, p-CHK1 and p-CHK2. γ-tubulin: loading control. **L.** Quantification of percentage of cells showing STN1 TIFs in *Pot1a*$^{-/-}$ and *Pot1b*$^{-/-}$ MEFs. **M.** Quantification of percentage of cells showing STN1 TIFs in WT MEFs with expressing sh*Trf2* or TPP1$^{\Delta RD}$. Scale bars 5μm.

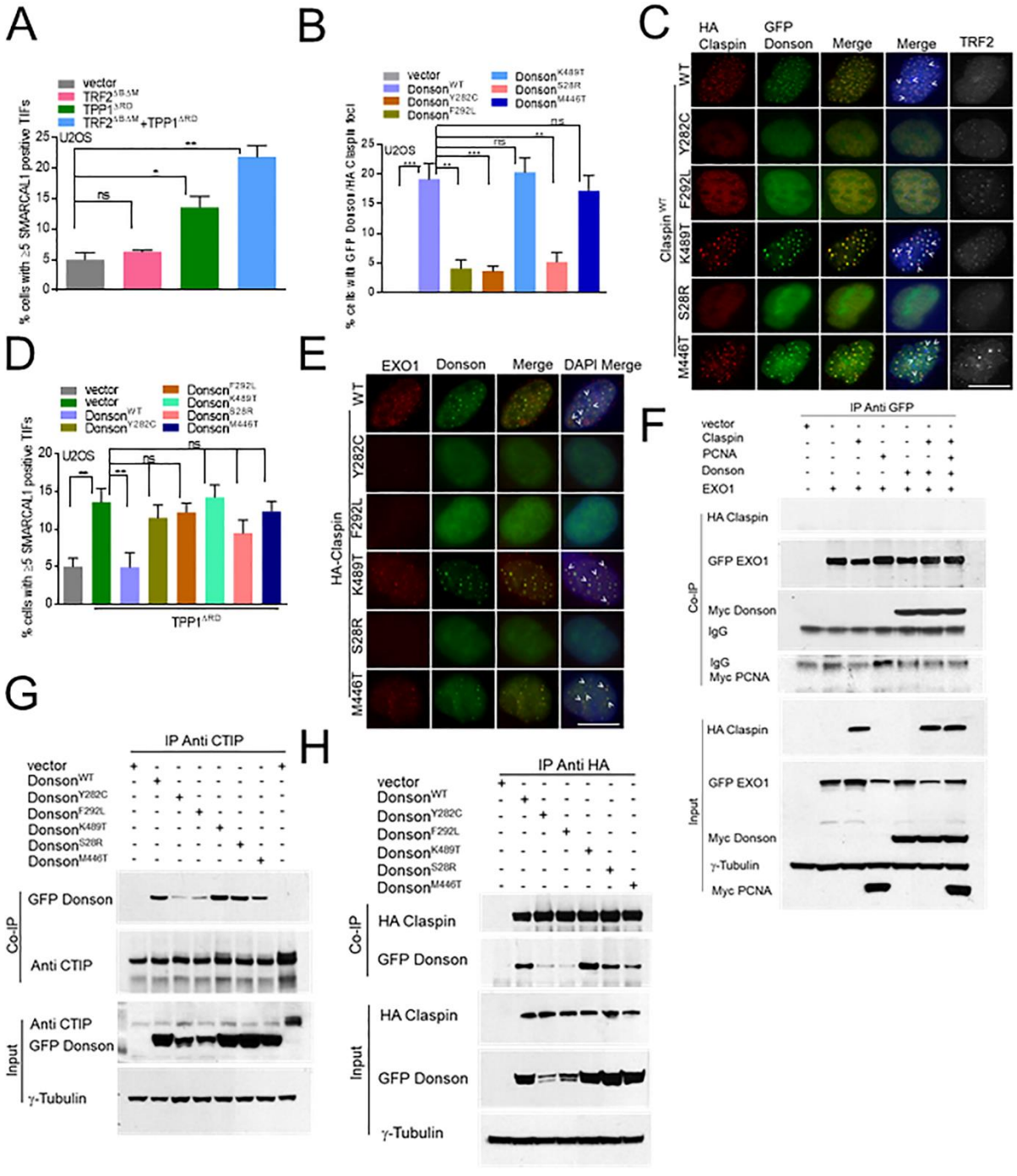
A
vector
TRF2ΔB.ΔM
TPP1ΔRD
TRF2ΔB.ΔM+TPP1ΔRD
U2OS
% cells with ≥5 SMARCAL1 positive TIFs
ns
*
**
B
vector
Donson WT
Donson Y282C
Donson F292L
Donson K489T
Donson S28R
Donson M446T
U2OS
% cells with GFP Donson/HA Claspin foci
ns
C
HA Claspin
GFP Donson
Merge
Merge
TRF2
Claspin WT
WT
Y282C
F292L
K489T
S28R
M446T
D
vector
vector
Donson WT
Donson Y282C
Donson F292L
Donson K489T
Donson S28R
Donson M446T
U2OS
% cells with ≥5 SMARCAL1 positive TIFs
ns
TPP1ΔRD
E
EXO1
Donson
Merge
DAPI Merge
HA-Claspin
WT
Y282C
F292L
K489T
S28R
M446T
F
IP Anti GFP
vector
Claspin
PCNA
Donson
EXO1
HA Claspin
GFP EXO1
Co-IP
Myc Donson
IgG
IgG
Myc PCNA
HA Claspin
GFP EXO1
Input
Myc Donson
γ-Tubulin
Myc PCNA
G
IP Anti CTIP
vector
Donson WT
Donson Y282C
Donson F292L
Donson K489T
Donson S28R
Donson M446T
Co-IP
GFP Donson
Anti CTIP
Input
Anti CTIP
GFP Donson
γ-Tubulin
H
IP Anti HA
vector
Donson WT
Donson Y282C
Donson F292L
Donson K489T
Donson S28R
Donson M446T
Co-IP
HA Claspin
GFP Donson
Input
HA Claspin
GFP Donson
γ-Tubulin
I
Claspin TBM motif
H. sapiens F V F H T L S P V K A E A
P. troglodytes F V F H T L S P V K A E A
M. mulatta F V F H T L S P V K A E A
B. taurus F V F H T L S P V K A E A
M. musculus F V F H T L S P T K A E A
G. gallus F V F H T L S P D K N E E

Figure S6: Related to Figure 6

A. Quantification of percentage of cells containing ≥ 5 SMARCAL1 TIFs. Data represents the mean of two independent experiments ± SD; n> 150 nuclei analyzed per experiment. **P*=0.01, ***P*=0.001 by one-way ANOVA. ns: non-significant. **B**. Quantification of co-localization of HA-Claspin with GFP-DONSON. Data represents the mean of two independent experiments ± SD; n>150 nuclei analyzed per experiment. ***P*=0.001, ****P*=0.0002 by one-way ANOVA. ns: non-significant. **C**. Co-localization of HA-Claspin with indicated GFP-DONSON disease mutations in transiently transfected U2OS cells. Anti-GFP antibody to visualize DONSON (green), anti-HA antibody to visualize Claspin (red), DAPI staining to visualize nuclei (blue). **D**. Quantification of percentage of cells containing ≥ 5 SMARCAL1-positive TIFs in U2OS cells expressing GFP-DONSON mutants and TPP1$^{\Delta RD}$. Data represents the mean of two independent experiments ± SD; n>150 nuclei analyzed per experiment. ***P*=0.001 by one-way ANOVA. ns: non-significant. **E**. Co-localization of endogenous EXO1 with WT GFP-DONSON and GFP-DONSON disease mutations transiently transfected in U2OS cells. Anti-GFP antibody was used to visualize DONSON (green), anti-EXO1 (red), DAPI staining to visualize nuclei (blue). **F**. Co-IP of GFP-EXO1 with HA-Claspin, Myc PCNA and Myc-DONSON in 293T cells using anti-GFP antibody. The inputs represent 5% of the total cell lysate used for the IP. γ-tubulin: loading control. **G**. Co-IP of WT GFP-DONSON and mutant GFP-DONSON with endogenous CTIP in 293T cells, using the anti-CTIP antibody. The inputs represent 5% of the total cell lysate used for the IP. γ -tubulin: loading control. **H**. Co-IP of WT GFP-DONSON and mutant GFP-DONSON with HA-Claspin in 293T cells, using anti-HA antibody conjugated agarose beads. The inputs represent 5% of the total cell lysate used for the IP. γ -tubulin: loading control. **I**. Conserved Claspin TBM (F/Y/H-X-L-X-P) residues (yellow) across the indicated species.

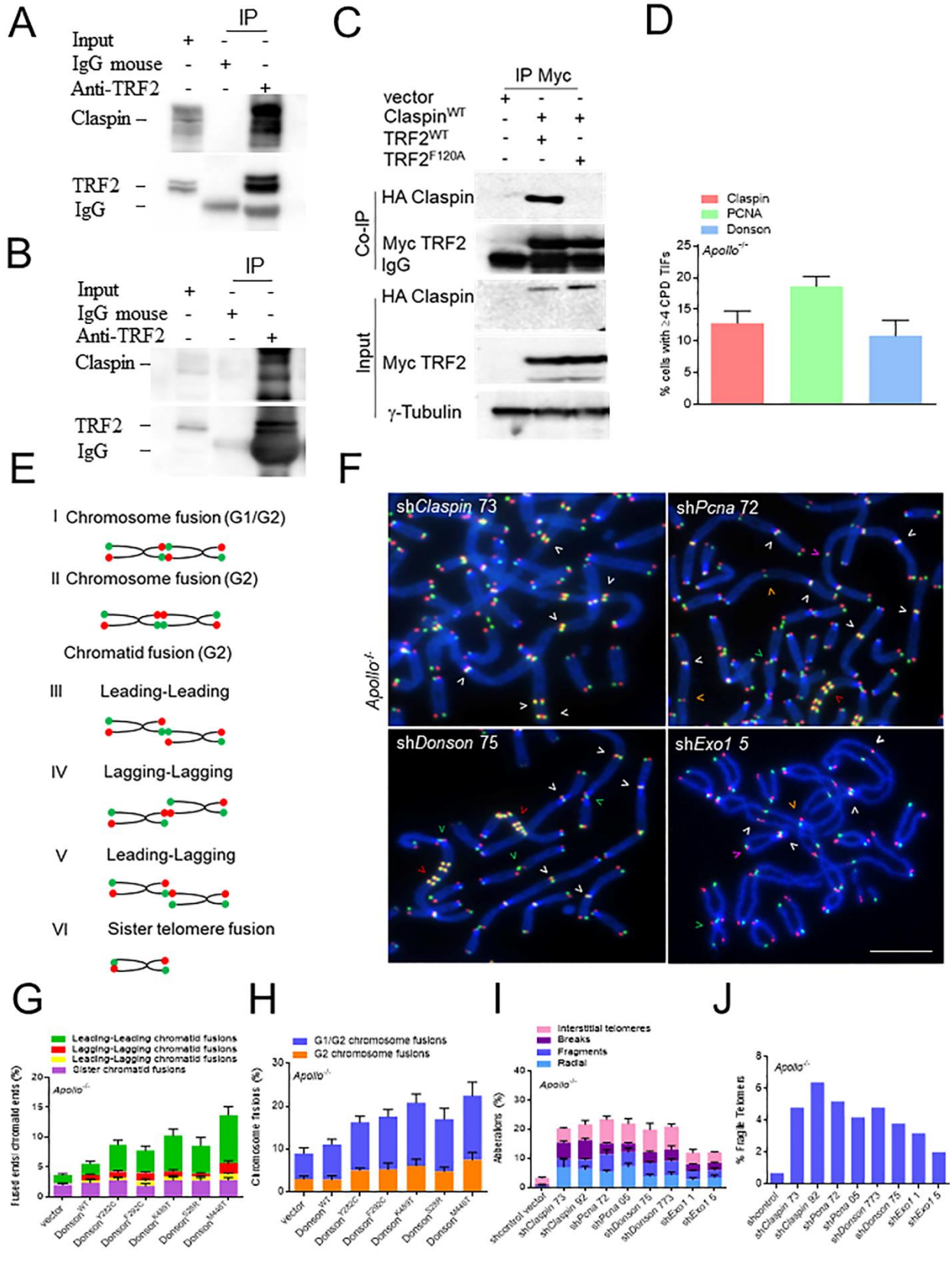
A
IP
Input + - -
IgG mouse - + -
Anti-TRF2 - - +
Claspin –
TRF2 –
IgG –
B
IP
Input + - -
IgG mouse - + -
Anti-TRF2 - - +
Claspin –
TRF2 –
IgG –
C
IP Myc
vector + - -
Claspin^WT - + +
TRF2^WT - + -
TRF2^F120A - - +
Co-IP
HA Claspin
Myc TRF2
IgG
Input
HA Claspin
Myc TRF2
γ-Tubulin
D
Claspin
PCNA
Donson
Apollo-/-
% cells with ≥4 CPD TIFs
25
20
15
10
5
0
E
I Chromosome fusion (G1/G2)
II Chromosome fusion (G2)
Chromatid fusion (G2)
III Leading-Leading
IV Lagging-Lagging
V Leading-Lagging
VI Sister telomere fusion
F
Apollo-/-
shClaspin 73
shPcna 72
shDonson 75
shExo1 5
G
Leading-Leading chromatid fusions
Lagging-Lagging chromatid fusions
Leading-Lagging chromatid fusions
Sister chromatid fusions
Apollo-/-
Fused ends/ chromatid ends (%)
vector
Donson WT
Donson T252C
Donson F292C
Donson K491T
Donson S28R
Donson M448T
H
G1/G2 chromosome fusions
G2 chromosome fusions
Apollo-/-
Chromosome fusions (%)
vector
Donson WT
Donson T252C
Donson F292C
Donson K491T
Donson S28R
Donson M448T
I
Interstitial telomeres
Breaks
Fragments
Radial
Apollo-/-
Aberrations (%)
shcontrol vector
shClaspin 73
shClaspin 92
shPcna 72
shPcna 05
shDonson 75
shDonson 773
shExo1 1
shExo1 5
J
Apollo-/-
% Fragile Telomeres
shcontrol
shClaspin 73
shClaspin 92
shPcna 72
shPcna 05
shDonson 773
shDonson 75
shExo1 1
shExo1 5

Figure S7: Related to Figure 6

Co-IP of endogenous Claspin using antibody against TRF2 in 293T (**A**) and *Nbs1*$^{-/-}$ MEFs (**B**). The inputs represent 5% of the total cell lysate used for the IP. γ-tubulin: loading control. **C**. Co-IP of HA-Claspin with Myc-TRF2^{WT} or Myc-TRF2^{F120A} with anti-Myc antibody conjugated agarose beads. The inputs represent 5% of the total cell lysate used for the IP. γ-tubulin: loading control. **D**. Quantification of the percentage of cells containing ≥ 4 CPD positive foci co-localizing with telomeres in *Apollo/SNM1B*$^{-/-}$ MEFs. **E**. Schematic of chromosome and chromatid fusions observed in *Apollo/SNM1B*$^{-/-}$ MEFs. **F**. *Apollo/SNM1B*$^{-/-}$ MEFs treated with indicated shRNAs for 120 h, after which metaphases were prepared and telomere fusions were visualized by CO-FISH. TelG-FAM, TelC-Cy3 and DAPI (blue) were used to visualize fused chromosomes (arrowheads). G1/G2 chromosome fusions (white arrows), G2 chromosome fusions (orange arrows), leading-leading (green), lagging-lagging (red), leading-lagging (yellow), sister-sister telomere fusion (pink). **G**. Quantification of chromatid-type and sister fusions in *Apollo/SNM1B*$^{-/-}$ MEFs expressing the indicated WT and GFP-DONSON mutants. Data represents the mean of two independent experiments as mean ± SD from 30 metaphases analyzed per experiment. **H**. Quantification of G1/G2 and G2 chromosome fusions in in *Apollo/SNM1B*$^{-/-}$ MEFs expressing the indicated WT and GFP-DONSON mutants. Data represents the mean of two independent experiments ± SD from 30 metaphases analyzed per experiment. **I**. Quantification of the number of interstitial telomere repeats, chromosome breaks, fragments and radial chromosomes in (**F**). Data represents the mean of two independent experiments ± SD from 50 metaphases analyzed per experiment. **J**. Quantification of fragile telomeres detected in (**F**)

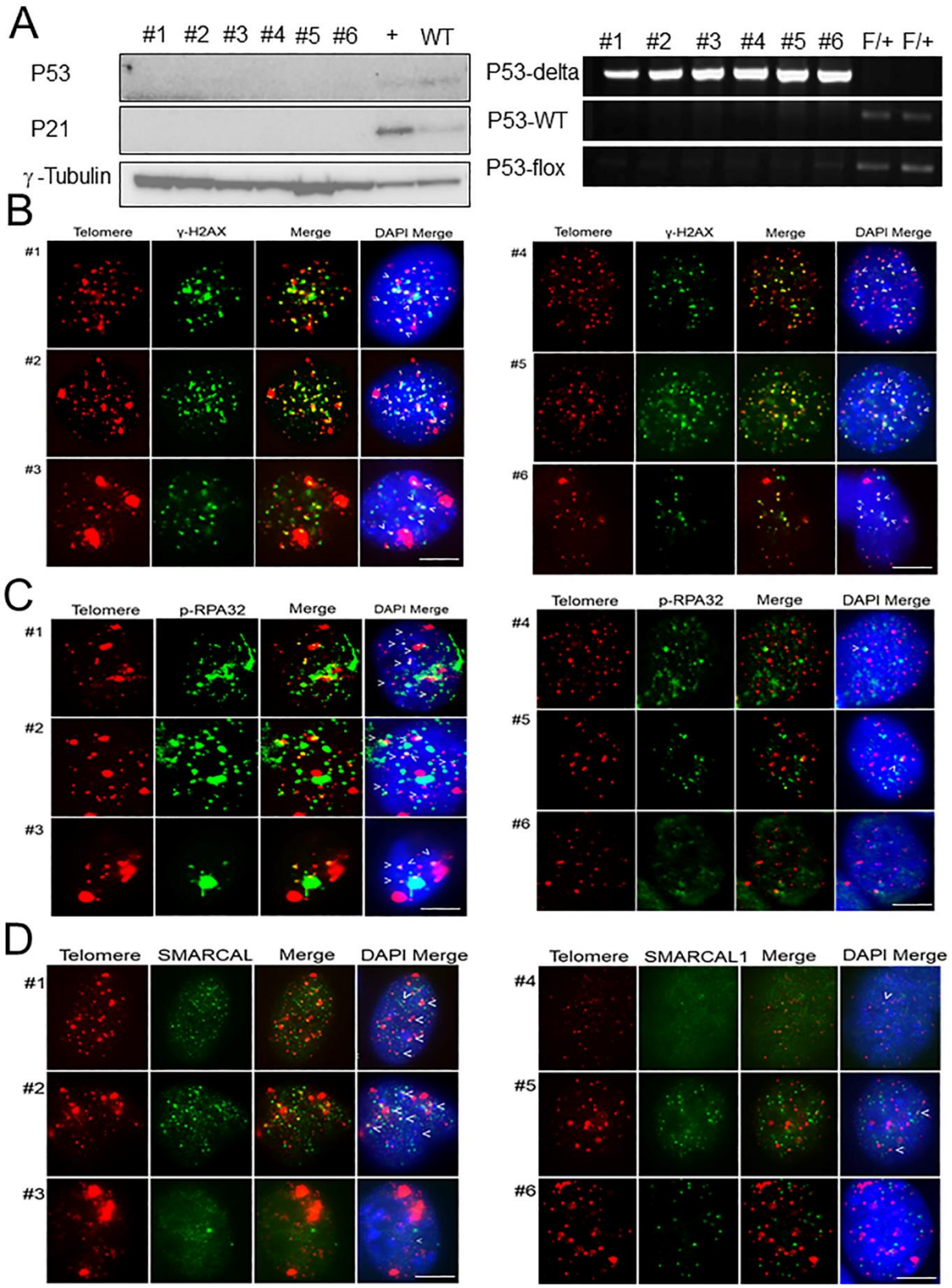
A
#1 #2 #3 #4 #5 #6 + WT
P53
P21
γ-Tubulin
#1 #2 #3 #4 #5 #6 F/+ F/+
P53-delta
P53-WT
P53-flox
B
Telomere γ-H2AX Merge DAPI Merge
#1
#2
#3
#4
#5
#6
C
Telomere p-RPA32 Merge DAPI Merge
#1
#2
#3
#4
#5
#6
D
Telomere SMARCAL Merge DAPI Merge
#1
#2
#3
Telomere SMARCAL1 Merge DAPI Merge
#4
#5
#6

Figure S8: Related to Figure 7

A. Immunoblot showing the loss of p53 and p21 expression in *MMTV-Cre*; $p53^{\Delta/\Delta}$; $Pot1a^{\Delta/\Delta}$ breast tumors (#1, 3, 4), sarcoma (#2) and salivary gland tumor (#5), breast tumor $p53^{\Delta/\Delta}$; $Pot1a^{F/\Delta}$ (#6). Lysates from $Ctc1^{-/-}$ spleen as positive control, WT spleen as negative control. γ-tubulin: loading control. Deletion of p53 floxed alleles in the tumors detected by PCR genotyping. $p53^{F/+}$ tail genomic DNA as positive control. **B-D.** Antibody against γ-H2AX, p-RPA32 and SMARCAL1 used to detect its co-localization with telomeres in tumor cell lines. Telomeres were visualized by PNA-FISH (red), antibody staining (green), and DAPI (blue). Scale bars 5μm.

Table S1: Details of tumor cell lines derived from mouse

Tumor cell lines	Mouse age when sacrificed (days)	Organs with tumor	Passages of cell lines when analyzed
#1	236	Mammal gland tumor	P38
#2	235	Sarcoma	P19
#3	382	Mammal gland tumor	P24
#4	339	Mammal gland tumor	P28
#5	339	Salivary solid tumor	P29
#6	308	Mammal gland tumor	P27